PUBLICATIONS OF THE ASTRONOMICAL SOCIETY OF THE PACIFIC, **119**: 994–1018, 2007 September

Absolute Calibration and Characterization of the Multiband Imaging Photometer for *Spitzer*. I. The Stellar Calibrator Sample and the 24 μm Calibration

C. W. ENGELBRACHT,[1] M. BLAYLOCK,[1] K. Y. L. SU,[1] J. RHO,[2] G. H. RIEKE,[1] J. MUZEROLLE,[1] D. L. PADGETT,[2] D. C. HINES,[3] K. D. GORDON,[1] D. FADDA,[2] A. NORIEGA-CRESPO,[2] D. M. KELLY,[1] W. B. LATTER,[4] J. L. HINZ,[1] K. A. MISSELT,[1] J. E. MORRISON,[1] J. A. STANSBERRY,[1] D. L. SHUPE,[2] S. STOLOVY,[2] WM. A. WHEATON,[2] E. T. YOUNG,[1] G. NEUGEBAUER,[1] S. WACHTER,[2] P. G. PÉREZ-GONZÁLEZ,[1,5] D. T. FRAYER,[2] AND F. R. MARLEAU[2]

Received 2006 November 15; accepted 2007 July 25; published 2007 September 28

ABSTRACT. We present the stellar calibrator sample and the conversion from instrumental to physical units for the 24 μm channel of the Multiband Imaging Photometer for *Spitzer* (MIPS). The primary calibrators are A stars, and the calibration factor based on those stars is 4.54×10^{-2} MJy sr^{-1} (DN s^{-1})$^{-1}$, with a nominal uncertainty of 2%. We discuss the data reduction procedures required to attain this accuracy; without these procedures, the calibration factor obtained using the automated pipeline at the *Spitzer* Science Center is 1.6% $\pm$ 0.6% lower. We extend this work to predict 24 μm flux densities for a sample of 238 stars that covers a larger range of flux densities and spectral types. We present a total of 348 measurements of 141 stars at 24 μm. This sample covers a factor of ~460 in 24 μm flux density, from 8.6 mJy up to 4.0 Jy. We show that the calibration is linear over that range with respect to target flux and background level. The calibration is based on observations made using 3 s exposures; a preliminary analysis shows that the calibration factor may be 1% and 2% lower for 10 and 30 s exposures, respectively. We also demonstrate that the calibration is very stable: over the course of the mission, repeated measurements of our routine calibrator, HD 159330, show a rms scatter of only 0.4%. Finally, we show that the point-spread function (PSF) is well measured and allows us to calibrate extended sources accurately; *Infrared Astronomy Satellite* (*IRAS*) and MIPS measurements of a sample of nearby galaxies are identical within the uncertainties.

1. INTRODUCTION

Space-based infrared astronomy satellites have used a variety of methods to perform flux calibration. For example, the *Infrared Astronomy Satellite* (*IRAS*; Beichman et al. 1988) extrapolated a ground-based 10 μm calibration out to 60 μm using stellar models and then used asteroids to transfer the 60 μm calibration to 100 μm. The *Midcourse Space Experiment* (*MSX*) was calibrated in a set of bands from ~8 to 20 μm using blackbodies ejected from the spacecraft itself (Price et al. 2004). The instruments aboard the *Infrared Space Observatory* (*ISO*) used a mix of astronomical sources, from stars for the *ISO* Camera (ISOCAM; Blommaert et al. 2003) to stars, asteroids, and planets for the *ISO* Photometer (ISOPHOT; Schulz et al. 2002) and Short Wavelength Spectrometer (SWS; Decin et al. 2000) and planets for the Long Wavelength Spectrometer (LWS; Gry et al. 2003). The Diffuse Infrared Background Experiment (DIRBE) imaged the sky in a series of bands from 1.25 to 240 μm and was calibrated against stars, planets, and planetary nebulae (Hauser et al. 1998). Like most of these missions, the instruments on board the *Spitzer Space Telescope* (Werner et al. 2004) are calibrated against celestial sources: for example, the Infrared Array Camera (IRAC; Fazio et al. 2004), with photometric bands from ~3 to 8 μm, is calibrated against stars (Reach et al. 2005), as is the Infrared Spectrograph (IRS; Houck et al. 2004).

The Multiband Imaging Photometer for *Spitzer* (MIPS; Rieke et al. 2004) has three photometric bands at 24, 70, and 160 μm. Like the other *Spitzer* instruments, the primary flux calibrators at 24 and 70 μm are stars; the calibrations are tied to the new infrared calibration by G. H. Rieke et al. (2007, in preparation) and are presented here (24 μm) and in a companion paper by Gordon et al. (2007b; 70 μm). The sensitivity of the 160 μm band is sufficient to allow it to be calibrated against stars, too,

[1] Steward Observatory, University of Arizona, Tucson, AZ; cengelbracht@as.arizona.edu, mblaylock@as.arizona.edu, ksu@as.arizona.edu, grieke@as.arizona.edu, jmuzerolle@as.arizona.edu, kgordon@as.arizona.edu, dkelly@as.arizona.edu, jhinz@as.arizona.edu, kmisselt@as.arizona.edu, jmorrison@as.arizona.edu, jstansberry@as.arizona.edu, eyoung@as.arizona.edu, gxn@as.arizona.edu.

[2] *Spitzer* Science Center, California Institute of Technology, Pasadena, CA; rho@ipac.caltech.edu, dlp@ipac.caltech.edu, fadda@ipac.caltech.edu, alberto@ipac.caltech.edu, shupe@ipac.caltech.edu, stolovy@ipac.caltech.edu, waw@ipac.caltech.edu, wachter@ipac.caltech.edu, frayer@ipac.caltech.edu, marleau@ipac.caltech.edu.

[3] Space Science Institute, Boulder, CO; dhines@as.arizona.edu.

[4] NASA *Herschel* Science Center, California Institute of Technology, Pasadena, CA; latter@ipac.caltech.edu.

[5] Current address: Departamento de Astrofísica, Facultad de CC. Físicas, Universidad Complutense de Madrid, Madrid, Spain; pgperez@as.arizona.edu.

but a strong, short-wavelength ghost image limits the accuracy with which such hot sources can be measured; hence, an asteroid-based transfer (and the color corrections required to make the transfer) of the stellar calibration from the shorter bands (similar in spirit to the *IRAS* 100 μm calibration) is presented in a companion paper by Stansberry et al. (2007).

The MIPS 24 μm calibration and capabilities can be compared to several previous missions that overlap in wavelength. For example, the quoted absolute calibration uncertainties of the large surveys performed by *IRAS* at 25 μm, by *MSX* at 21 μm, and by DIRBE at 25 μm are 8% (Beichman et al. 1988), 7% (Cohen et al. 2001), and 15% (Hauser et al. 1998), respectively. These missions were optimized for large area surveys and used older detector technology. As a result, the beam size and point-source detection limits are poor compared to the *Spitzer* and *ISO* pointed observatories. Like MIPS, the ISOPHOT instrument was designed as a general-user instrument, but the 25 μm channel (which achieved an accuracy of ~10%; Klaas et al. 2003) was an aperture photometer and not capable of imaging. Thus, MIPS is the first space instrument with an array detector optimized for imaging near 24 μm, achieving a point-source sensitivity of ~60 μJy (5 σ, 2000 s; *Spitzer* Observer's Manual), with a beam of 6″ FWHM. As we show in this paper, the absolute calibration of the MIPS 24 μm channel is accurate to 2%, which has expanded the science possible in this wavelength range. For example, the MIPS 24 μm channel allows measurement of infrared excesses around stars with lower effective temperatures and/or lower mass debris disks than previously possible (e.g., Rieke et al. 2005; Bryden et al. 2006).

Careful data reduction procedures are essential to reproduce the results presented here; accordingly, we discuss the data reduction and photometry in some depth in § 2. The calibration factor itself is computed in § 3. To explore the quality of the calibration, we expand the sample of targets beyond those used to measure the calibration factor; the details of the flux prediction are presented in § 4. We use the expanded sample in a series of tests of the calibration, discussed in § 5. Finally, we summarize our results in § 6.

2. DATA REDUCTION AND PHOTOMETRY

2.1. Standard Processing

The data were all obtained using the MIPS small-field photometry mode astronomical observation template (AOT). For most targets, two cycles of photometry using 3 s exposures were obtained, resulting in 14 individual images at each of two telescope nod positions (excluding the short exposure that starts the data-taking sequence at each of the two telescope nod positions). Starting with the raw data downloaded from the *Spitzer* Science Center (SSC), these data were processed using version 3.06 of the MIPS Data Analysis Tool (DAT; Gordon et al. 2005), which performs standard processing of infrared detector array data (slope fitting, dark subtraction, linearity correction, flat fielding, and mosaicking), as well as steps specific to the array used in MIPS (droop correction and dynamic range extension using the first difference frame)—these steps are described in more detail in that paper. Experience gained with the flight instrument has prompted the application of additional processing, not discussed by Gordon et al. (2005), to remove low-level instrumental artifacts. In particular, one of the four readouts on the array can incur an offset of several counts per second (due to a bright source or cosmic ray on detectors connected to that readout) relative to the other three, resulting in a striping effect (dubbed "jailbar")—an additive correction is applied to that readout to remove the effect. In addition, the in-orbit flat field has several dark spots (due to particulate matter on the pick-off mirror) that shift position on the array as the scan mirror (which imposes small pointing adjustments as part of the normal observing sequence) moves. To remove these spots, a flat field specific to scan mirror position is applied as part of the standard processing. These artifacts are illustrated in Figure 1.

2.2. Additional Processing

There are additional low-level artifacts present in the MIPS data after the standard processing described above has been applied. We assess the severity of these effects and correct those that have a significant effect on our measurements. In roughly decreasing order of importance, these artifacts are:

The MIPS 24 μm array is subject to medium-term (~1 week) gain changes that affect pixels that have been exposed to highly saturating sources, at the level of a few percent. A typical MIPS 24 μm observation will have several regions that have been affected this way as the cumulative result of normal operations during that instrument campaign. An additional flat field, made from a median stack of the data with the source masked out, is applied to remove the gain changes.

Background levels observed by MIPS at 24 μm can change by several counts per second from image to image throughout an observing sequence, likely due to scattered zodiacal light that depends on the position of the MIPS scan mirror. Uncorrected, this can affect the photometry of our faintest (~10 mJy) calibrators at the level of ~1%. To mitigate this effect, we subtract the median level (after masking the source) from each image before mosaicking.

Any source that falls on the MIPS 24 μm array leaves a residual image of about 0.5% that decays with a timescale of roughly 10 s. The dither pattern used in the photometry AOT ensures that the source falls on a different part of the array after every exposure, and thus any residual image has decayed to a small fraction of a percent by the time the new source position is within several FWHMs of a previous position. Residual images have a negligible effect on the calibration factor that we derive here, and we perform no correction for them.

Sources that saturate the MIPS 24 μm array in the full (3 s) exposures used here can affect the offset of the pixels read out

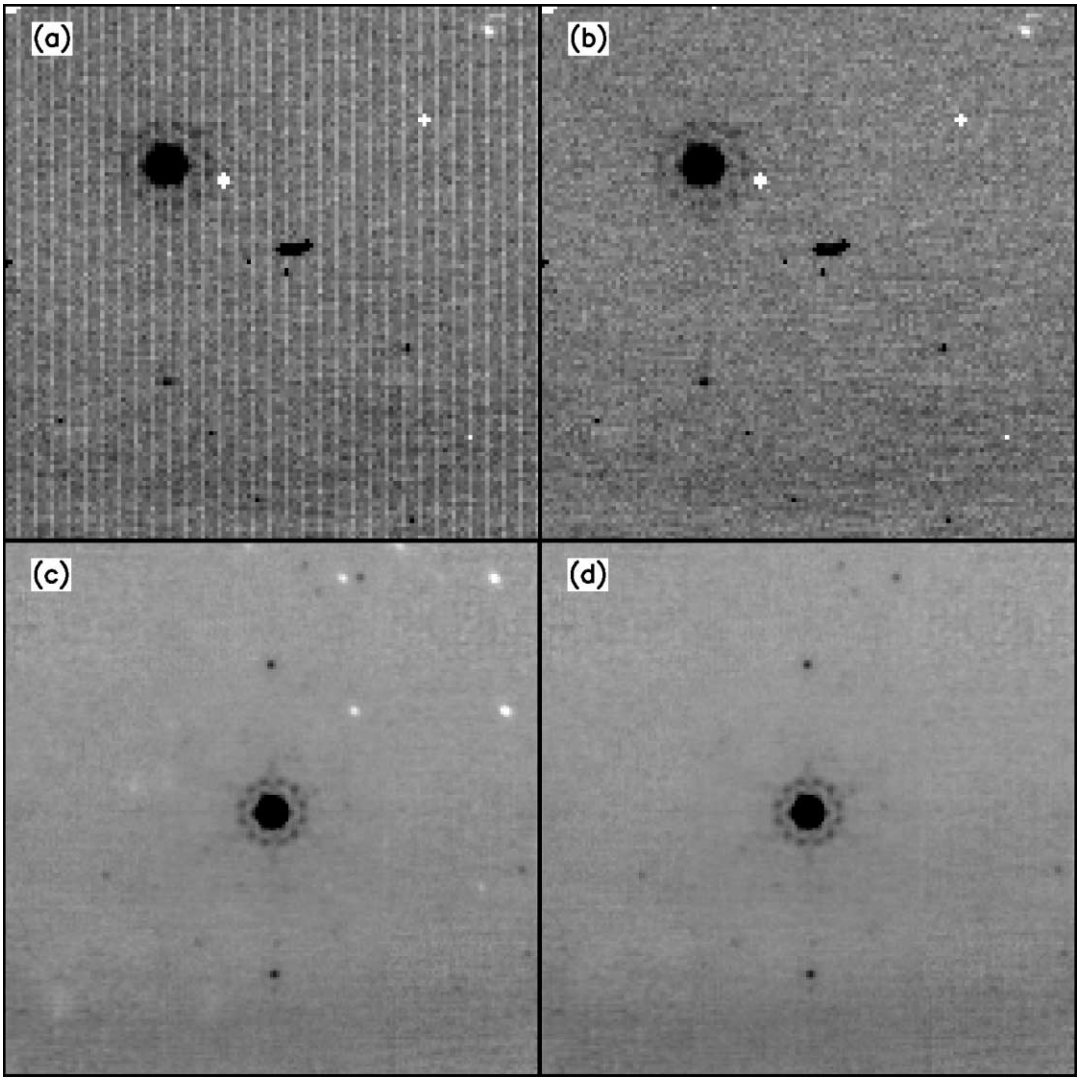

FIG. 1.—Artifacts not discussed by Gordon et al. (2005) that are now fixed as part of standard processing with the MIPS Data Analysis Tool (DAT), illustrated using observations of HD 159330 (AOR key 13587712) plotted in reverse gray scale. (*a*) The jailbar effect is most easily seen in individual frames, here caused by a cosmic ray below and to the right of the star, and (*b*) fixed as described in § 2. (*c*) The spots caused by debris on the pick-off mirror (several sharp white spots above and to the right of the star, as well as diffuse white regions below and to the left of the star) are most easily seen in a mosaicked image and are (*d*) fixed using separate flat fields for each scan mirror position.

after the ones on the source and can even change the magnitude of the jailbar effect on those pixels, resulting in a different striping pattern above and below the source on the array. The offset is a few counts per second and only occurs for the brightest sources, so it has a negligible effect on the photometry of those sources and we make no correction here.

Examples showing the artifacts discussed here are shown in Figure 2.

2.3. Mosaicking

After applying the corrections discussed above, we co-add the data to make a mosaic image of each source. As the natural unit of a flat-fielded image is surface brightness, the mosaicking step conserves surface brightness as it removes optical distortions. The final images have square pixels 2.45″ on a side, very similar to the natural pixel width near the center of the array, 2.49″. The source positions in the photometry AOT range over the central 2.5′ of the array; to ensure that there are no calibration changes across the full array, we have tested the distortion correction on individual images. Using the `phot` task in the Image Reduction and Analysis Facility (IRAF),[6] we compared photometry in a

[6] IRAF is distributed by the National Optical Astronomy Observatory, which is operated by the Association of Universities for Research in Astronomy, Inc., under cooperative agreement with the National Science Foundation.

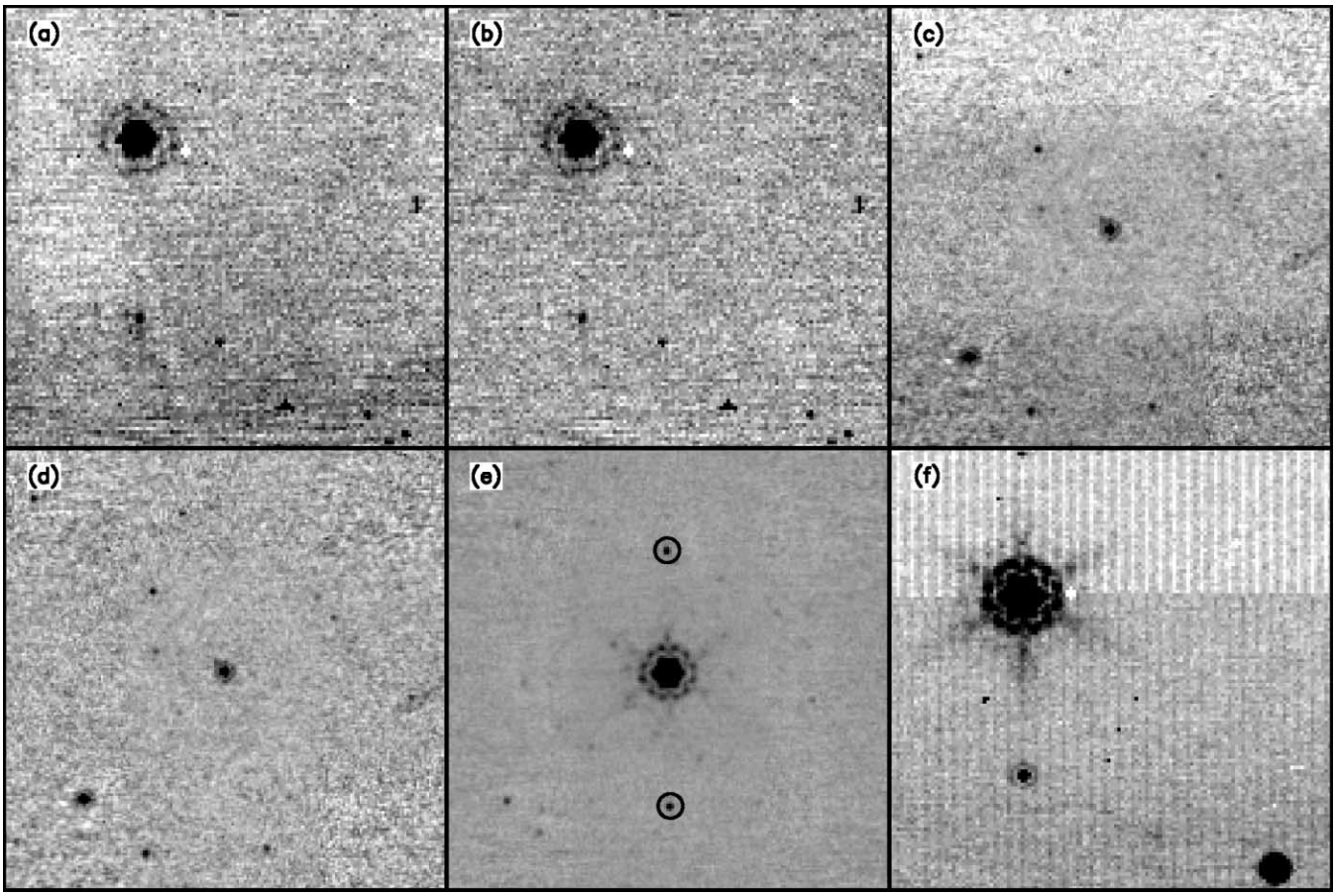

FIG. 2.—Artifacts not removed by standard processing with the MIPS DAT, plotted in reverse gray scale. As discussed in § 2, (*a*) gain changes imposed by previous observations (illustrated using a single-frame observation of HD 159330, AOR key 12195328) are (*b*) removed using a second flat field. (*c*) Background changes as a function of scan mirror position (illustrated using a mosaic observation of HD 106965, AOR key 13201920) are (*d*) removed before mosaicking. For the targets discussed here, the effects of (*e*) residual images (*circled*; illustrated using a mosaic observation of HD 159330, AOR key 12195328) and (*f*) sources that saturate in 3 s (illustrated using a single-frame observation of HD 180711, AOR key 9805568) are small and we make no correction.

fixed aperture (6 pixels in radius, with a background annulus from 7 to 12 pixels) for 416 measurements of HD 042082 made during a focal plane survey that positioned the star over the full extent of the array. Without correction for distortion, the measured counts increased smoothly by 12% from the upper left-hand corner of the array to the lower right-hand corner of the array, inversely proportional to the 12% change in pixel area, from 6.91 to 6.11 arcsec^2. As expected, correcting the images for distortion eliminates this trend, resulting in a 1 σ dispersion in the measurements of only 0.8%.

2.4. Photometry

To compute aperture corrections for photometry, we make use of a point-response function (PRF) constructed as follows. We start with a point-spread function (PSF) of a 10,000 K blackbody (the spectral energy distributions of the stars that we use to calibrate differ negligibly from this at 24 μm) generated using the *Spitzer* TinyTim software (STinyTim; Krist 2002). The PSF is computed at the center of the array using an image size (10′ width) large enough to encompass >99% of the light. We "observe" the model using the MIPS simulator (software designed to simulate MIPS data, including optical distortions, using the same observing templates used in flight) and mosaic the simulated data using the same software with which we processed the real data. We compare the result to one of the calibration stars in Figure 3. The structure predicted by the model, down to very faint levels and in the diffraction spikes, is very similar to what is observed on a real star. Additional insight is gained from a comparison of radial profiles (Fig. 4), where it can be seen that the model is an excellent description of the data, out to the third Airy ring. A similar, and slightly improved, fit to the radial profile can be obtained by smoothing the STinyTim model by the equivalent of a boxcar 1.8 pixels in width (possibly indicating a small amount of pointing jitter or scattered light, neither of which is modeled by the simulator). We apply the `phot` task in IRAF to

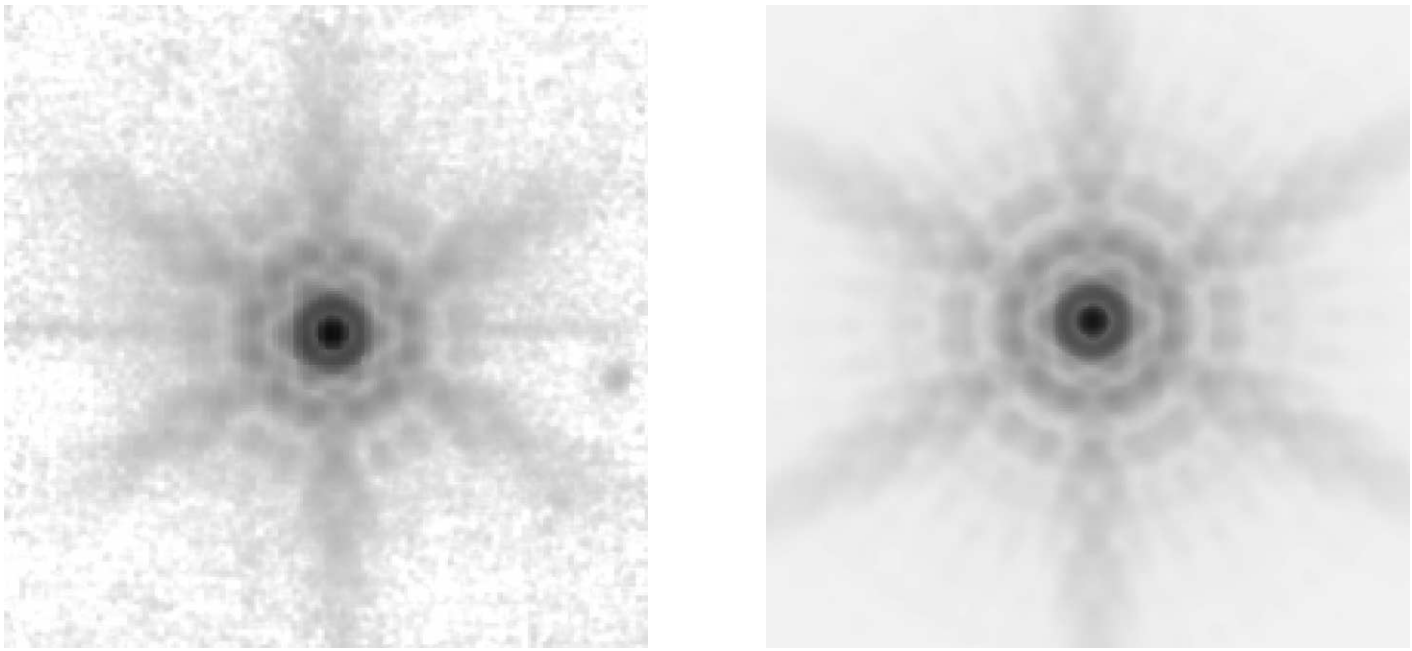

FIG. 3.—Comparison of observed and model PSF, plotted in reverse gray scale. *Left:* Image of HD 009927; the horizontal feature through the center of the image is a detector artifact. The dynamic range (from the peak brightness of 60,000 DN s^{-1} to the 1 σ noise level of 3 DN s^{-1}) is 20,000. *Right:* Model generated by StinyTim, after processing through the MIPS simulator (see § 2.4). Both images have been heavily compressed using an asinh transform to show faint structure, and the gray-scale levels have been adjusted by eye to match each other.

the boxcar-smoothed image to compute the aperture corrections, representative values of which are shown in Table 1. We find that the counts measured by various photometry routines vary by ~1%, so we assign a 1% uncertainty to the aperture correction.

We perform aperture photometry on the observations using an aperture 35″ in radius, with a background annulus from 40″ to 50″ in radius. This aperture is large enough to minimize uncertainties due to centroiding errors and to ensure that any uncertainties in the aperture correction have a small effect on the derived counts. We derive the uncertainty on each measurement from the scatter of the pixel values in the background aperture. The measurements are listed in Table 2.

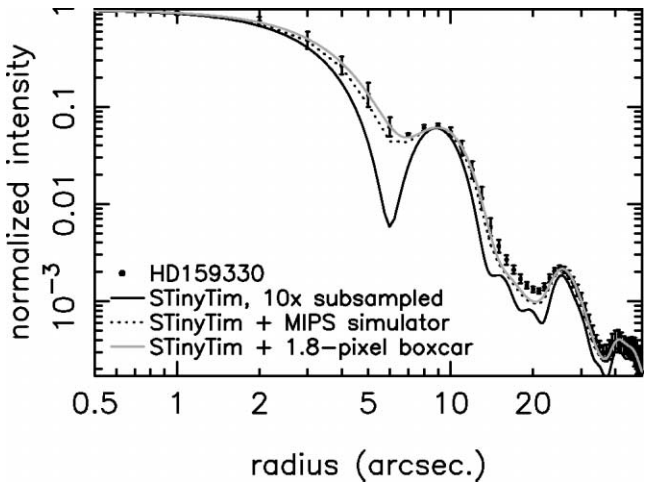

FIG. 4.—Radial profile of a star (*points*), compared to a 10 × subsampled model profile generated by STinyTim (*black solid line*), along with that same model profile run through the MIPS simulator (*black dotted line*; see § 2 for details) or smoothed by a 1.8 pixel boxcar (*gray solid line*).

2.5. Comparison to SSC Pipeline

We compare the measurements made on data reduced using the DAT to those obtained using identical photometry procedures on data processed using the automated pipeline at the SSC, which does not apply the second flat field (made using a median stack of the data; see § 2.2) or the background subtraction. We convert the units of the SSC data products from MJy sr^{-1} to DN s^{-1} by dividing by the `FLUXCONV` value found in the header. Based on 90 measurements of HD 159330 processed using the S15.3.0 version of the pipeline, we find that the count rate in the pipeline-reduced data is 1.6% ± 0.6% higher than in data reduced using the DAT. The difference between the reductions is marginally significant (2.7 σ) and may be due to the extra processing steps applied to the DAT-processed data.

2.6. Scan Map Calibration

The results that we present here rely on measurements of calibrator stars performed using the photometry AOT, which images the sky in a nod-and-stare pattern. MIPS has a second

TABLE 1
24 μm Aperture Correction Factors for a 10,000 K Blackbody

Description	Radius (arcsec)	Background Annulus (arcsec)				
		6–8	7–13	20–32	40–50	None
Half first dark ring	3.5	2.78	2.80	2.57	2.56	2.56
Center of first dark ring	7.0	...	2.05	1.61	1.61	1.61
Outside first bright ring	13.0	...	...	1.17	1.16	1.16
Center of second dark ring	20.0	...	...	1.15	1.13	1.12
Outside second bright ring	35.0	...	...	...	1.08[a]	1.06

[a] Aperture correction used for calibration.

imaging mode, the scan map AOT, which images the sky using a continuous track of the spacecraft. The scan mode uses the same optical train as the photometry mode, so we expect that the calibration derived here would apply equally to both modes. To check whether subtle differences exist in the shape of the PSF that might affect the calibration, we compare photometry in scan and photometry modes on two stars observed in multiple epochs, HD 159330 and HD 163588. We find that the radial profiles in scan and photometry modes are identical within the uncertainties and that photometry in these two modes agrees within ~1%, confirming that the photometry calibration is applicable to scan-mode data. Similar results were found by Fadda et al. (2006).

3. THE 24 μm CALIBRATION FACTOR

Following G. H. Rieke et al. (2007, in preparation) we base the flux calibration of the MIPS 24 μm band on A stars. We adopt the sample of 22 A stars from G. H. Rieke et al. (2007, in preparation), as a consistent suite of measurements is available for these targets and the sample has already been vetted for sources that would bias the calibration, such as those with an infrared excess. Here and throughout this work, monochromatic flux densities are computed at 23.675 μm, the effective wavelength of the 24 μm band, although we continue to use the shorthand "24 μm" for convenience. We compute 24 μm flux densities using the extinction-corrected K_s magnitudes computed by G. H. Rieke et al. (2007, in preparation), a $K_s - [24]$ color difference of 0 mag, and the 24 μm (i.e., 23.675 μm) zero point derived by G. H. Rieke et al. (2007, in preparation) of 7.17 Jy. We apply the aperture correction derived in § 2 (1.08) to the measurements from Table 2, averaging multiple measurements when available. The counts in that table are integrations over an aperture, so we convert the implied unit of "pixel" (that we have ignored thus far) to an angular area using the pixel size (2.45″ on a side) of our mosaics. The calibration factor is the weighted average of the ratio of the 24 μm predictions to the observed count rate, or 4.54×10^{-2} MJy sr^{-1} (DN s^{-1})$^{-1}$, with a formal uncertainty of 0.7%. At the pixel scale of our mosaics, this factor is equivalent to 6.40×10^{-6} Jy pixel^{-1} (DN s^{-1})$^{-1}$ (which can be converted to other pixel scales by multiplying by the square of the ratio of the pixel size to 2.45″). Following G. H. Rieke et al. (2007, in preparation) we assign an uncertainty of 2% to the calibration factor to allow for systematic effects in propagating the near-infrared measurements to 24 μm. Where care is taken to apply the corrections discussed in § 2 and to treat calibration stars and other targets in a consistent manner, this calibration accuracy can be maintained in science data. The data used to compute the calibration factor are summarized in Table 3.

The calibration factor was derived using stars, and no color corrections were applied to the measurements used here. Stars are relatively blue ($f_\nu \propto \nu^{-2}$) at MIPS wavelengths, so color corrections are required to calibrate sources with different spectral distributions. As shown by Stansberry et al. (2007), however, these corrections are small in the MIPS 24 μm band: they are no more than 3% over a range of power-law indices (−3 to 3) and do not exceed 5% for blackbody sources above a temperature of 57 K.

4. SAMPLE AND PREDICTED FLUXES

The sample of stars used in § 3 to derive the 24 μm calibration factor covers a limited dynamic range and is too small to statistically probe characteristics of the instrument behavior such as linearity and the effects of sky brightness. Furthermore, these stars are too faint to be useful as calibrators for the MIPS 70 μm band (discussed by Gordon et al. 2007b). In this section, we develop an expanded sample of 24 μm calibrators to support our characterization of the performance of the instrument, which we discuss in § 5. These stars were selected to explore the dynamic range of the instrument within reasonable integration times and to probe the effects of spectral type and environment (primarily foreground/background level) on the calibration.

4.1. Zero-Point Conversions for Additional Data Sets

We predict flux densities at 24 μm for the expanded MIPS calibration target list by extrapolating measurements made at near- and mid-infrared wavelengths. The scale factors for the Two Micron All Sky Survey (2MASS; Skrutskie et al. 2006) measurements of A and G stars made in the read-1 (the 51 ms exposure used to measure sources that saturate the full 1.3 s exposure) data are given by G. H. Rieke et al. (2007, in preparation), who find that $K_s - [24]$ is 0 (by definition) and 0.045 ± 0.011 mag, respectively. The 2MASS read-1 magnitude limit (~3.5 mag at K_s) is not low enough to constrain

TABLE 2
24 μm MEASUREMENTS OF MIPS FLUX CALIBRATORS

Name	Days Since Mission Start	AOR Key[a]	DCE[b] Time (s)	Count Rate (DN s^{-1})	Uncertainty (DN s^{-1})
BD +621644	496.4	13071616	3	1.033E+04	5.19E+01
HD 000319	300.4	3972864	3	6.708E+03	5.00E+01
HD 001160	322.3	10090496	3	1.395E+03	1.56E+01
HD 001644	322.3	10090752	3	8.191E+03	5.69E+01
HD 002151	806.5	16276992	3	3.271E+05	1.23E+03
HD 002811	298.4	9940224	3	1.591E+03	3.35E+01
HD 008941	359.7	5414400	3	7.202E+03	3.46E+01
HD 009927	871.5	16619776	3	6.045E+05	2.45E+03
HD 011413	298.5	3973376	3	7.866E+03	3.87E+01
HD 014943	298.4	9940480	3	7.180E+03	2.84E+01
HD 015008	69.4	7345408	3	2.698E+04	1.14E+02
	84.0	7979264	3	2.662E+04	1.09E+02
	1133.7	20460800	3	2.672E+04	5.28E+01
	1133.6	20461056	30	2.730E+04	1.51E+01
	1133.7	20461312	10	2.705E+04	2.31E+01
HD 015646	394.6	3973888	3	2.997E+03	4.84E+01
HD 017254	339.7	11783424	3	4.482E+03	2.75E+01
	466.2	12871936	3	4.578E+03	2.81E+01
	1133.6	20462848	3	4.649E+03	5.28E+01
	1133.6	20463104	10	4.575E+03	2.31E+01
	1133.6	20463360	30	4.689E+03	1.44E+01
HD 019019	367.9	5407744	3	6.204E+03	3.74E+01
HD 020722	386.5	12063488	3	5.818E+03	4.56E+01
HD 020888	339.7	11783680	3	5.624E+03	2.99E+01
	630.9	13613568	3	5.427E+03	2.79E+01
HD 020902	905.8	16868864	3	6.872E+05	2.62E+03
HD 021981	153.6	8812544	10	6.089E+03	1.33E+01
HD 025860	702.7	15421440	3	4.202E+03	3.26E+01
HD 027466	392.1	5412096	3	3.146E+03	3.18E+01
HD 028099	762.9	15991808	3	2.546E+03	2.80E+01
HD 028471	181.1	9059072	10	3.173E+03	1.81E+01
HD 029461	762.9	15992064	3	2.759E+03	2.77E+01
HD 030246	762.9	15992320	3	2.497E+03	2.75E+01
HD 032831	386.4	12062464	3	2.301E+05	8.06E+02
HD 034868	179.9	3983360	3	3.851E+03	3.89E+01
HD 035666	364.2	11891968	3	3.416E+04	1.34E+02
HD 036167	920.0	16869120	3	5.627E+05	2.23E+03
HD 037962	414.8	5412864	3	3.281E+03	3.12E+01
HD 038949	416.4	5340160	3	2.871E+03	3.10E+01
HD 039608	61.0	7200768	3	3.844E+04	1.49E+02
	69.9	7743232	3	3.832E+04	1.46E+02
	84.0	7977472	3	3.805E+04	1.43E+02
	1133.7	20460032	3	3.780E+04	5.19E+01
	1133.7	20460288	10	3.842E+04	2.38E+01
	1133.7	20460544	30	3.878E+04	1.56E+01
HD 040129	386.5	12062720	3	2.025E+03	2.04E+01
HD 040335	202.7	9192192	3	2.866E+03	3.25E+01
HD 041371	386.5	12062976	3	1.491E+04	7.41E+01
	1133.7	20461568	10	1.494E+04	2.29E+01
	1133.7	20461824	30	1.502E+04	1.42E+01
	1133.7	20463616	3	1.462E+04	5.06E+01
HD 042525	631.5	13588224	3	5.116E+03	2.85E+01
HD 042701	35.3	6772992	3	4.363E+04	1.79E+02
	228.2	9457920	3	4.333E+04	1.61E+02
HD 043107	34.1	6765056	3	7.581E+03	1.05E+02
	34.1	6765312	10	7.757E+03	7.84E+01
	34.1	6765568	30	8.214E+03	7.31E+01
	34.1	6765824	3	8.087E+03	6.96E+01
	69.5	7342080	3	8.176E+03	6.96E+01
	69.5	7342336	10	8.386E+03	5.52E+01
	69.5	7344640	3	8.373E+03	1.64E+01

TABLE 2 (*Continued*)

Name	Days Since Mission Start	AOR Key[a]	DCE[b] Time (s)	Count Rate (DN s^{-1})	Uncertainty (DN s^{-1})
	69.5	7344896	3	8.104E+03	2.50E+01
	69.2	7346944	3	8.090E+03	6.99E+01
	69.3	7347200	3	7.298E+04	3.53E+02
	69.3	7347968	3	8.048E+03	6.92E+01
	91.8	7866112	3	8.122E+03	6.60E+01
	91.8	7866368	3	7.984E+04	4.24E+02
	91.8	7867136	3	8.206E+03	6.32E+01
HD 044594	70.6	7339008	3	9.411E+03	4.79E+01
HD 045557	631.5	13588480	3	5.492E+03	3.51E+01
HD 046190	258.0	9662976	3	3.703E+03	2.82E+01
HD 046819	393.7	12063232	3	8.504E+03	4.94E+01
HD 047332	364.2	11892224	3	2.595E+03	2.60E+01
HD 050310	205.7	9192448	3	7.865E+05	2.88E+03
HD 053501	35.3	6773248	3	1.837E+05	6.89E+02
	60.9	7199232	3	1.840E+05	6.66E+02
	69.9	7742976	3	1.840E+05	7.02E+02
	84.0	7977728	3	1.831E+05	1.06E+03
HD 057336	631.5	13588736	3	1.403E+03	3.44E+01
HD 058142	49.7	7145472	3	1.458E+04	1.33E+02
HD 060178	228.2	9458176	3	2.584E+05	7.17E+02
HD 061929	631.5	13588992	3	3.038E+03	2.66E+01
HD 064324	416.9	5400832	3	3.672E+03	3.87E+01
HD 065517	631.6	13589248	3	2.122E+03	1.81E+01
HD 066751	416.2	5409280	3	9.671E+03	2.80E+01
HD 069863	631.5	13589504	3	1.240E+04	5.52E+01
HD 073210	226.2	3986432	3	3.707E+03	5.55E+01
HD 073666	227.7	3986688	3	2.541E+03	5.66E+01
HD 073819	226.2	3987200	3	3.170E+03	5.29E+01
HD 077281	627.2	13589760	3	1.673E+03	1.99E+01
HD 080007	319.4	10091008	3	2.592E+05	9.55E+02
	339.8	11783936	3	2.596E+05	9.23E+02
HD 082308	97.0	7973888	3	7.022E+05	2.59E+03
HD 082621	70.6	7338496	3	1.909E+04	8.24E+01
HD 087901	96.9	7972096	3	2.350E+05	7.87E+02
HD 091375	258.0	9663232	3	1.602E+04	6.73E+01
HD 092788	494.8	5440512	3	5.299E+03	3.93E+01
HD 092845	301.2	3990016	3	7.166E+03	4.51E+01
HD 096833	97.0	7974144	3	7.470E+05	2.80E+03
	869.7	16619008	3	7.373E+05	3.09E+03
HD 098230	869.7	16619264	3	1.467E+05	4.65E+02
HD 098553	301.2	5408512	3	3.858E+03	3.39E+01
HD 100167	463.9	5420544	3	5.036E+03	3.57E+01
HD 101452	664.8	15247104	3	1.910E+03	3.50E+01
HD 101472	518.8	5343232	3	3.834E+03	3.44E+01
HD 101959	301.2	5419008	3	5.822E+03	3.20E+01
HD 102647	302.5	9940736	3	2.372E+05	7.01E+02
	869.7	16618752	3	2.358E+05	7.39E+02
HD 102870	298.4	9940992	3	1.309E+05	5.02E+02
HD 105805	278.5	3991808	3	5.734E+03	5.10E+01
HD 106252	284.1	5442816	3	4.749E+03	3.73E+01
HD 106965	521.7	13201920	3	1.248E+03	1.87E+01
HD 108799	322.4	5338624	3	1.242E+04	4.16E+01
HD 108944	518.7	5334784	3	4.431E+03	3.10E+01
HD 109612	524.6	13111808	3	1.260E+04	6.56E+01
HD 109866	524.9	13112064	3	4.368E+03	2.77E+01
HD 110304	905.9	16869376	3	1.510E+05	5.70E+02
HD 112196	492.2	5278976	3	6.345E+03	3.41E+01
HD 115043	281.5	6599168	3	7.863E+03	3.29E+01
HD 115780	563.2	13380864	3	1.022E+04	1.25E+02
	563.3	13383680	3	1.064E+04	1.38E+02
HD 116706	279.6	3994624	3	6.188E+03	5.01E+01
HD 119545	551.8	13313024	3	1.360E+05	2.33E+03
HD 121370	905.8	16836608	3	3.132E+05	1.17E+03

TABLE 2 (*Continued*)

Name	Days Since Mission Start	AOR Key[a]	DCE[b] Time (s)	Count Rate (DN s^{-1})	Uncertainty (DN s^{-1})
HD 121504	340.5	5438208	3	4.016E+03	4.34E+01
HD 122652	302.0	5428224	3	5.100E+03	2.87E+01
HD 123123	905.9	16869632	3	6.343E+05	2.39E+03
HD 127665	181.2	9059328	3	6.687E+05	2.51E+03
HD 128998	671.5	15247360	3	4.824E+03	2.79E+01
HD 129655	705.6	15421696	3	2.577E+03	2.87E+01
HD 131986	551.8	13313280	3	7.721E+03	9.91E+01
HD 132417	551.7	13313536	3	5.041E+03	5.49E+01
HD 132439	551.7	13313792	3	5.055E+03	3.77E+01
HD 134493	202.1	9191936	3	2.956E+04	1.24E+02
HD 138265	96.9	7972352	3	1.447E+05	5.20E+02
	202.1	9191680	3	1.443E+05	7.25E+02
HD 139698	551.7	13314048	3	8.006E+03	1.99E+02
HD 141937	345.4	5442048	3	5.126E+03	3.82E+01
HD 144873	671.6	15247616	3	1.723E+03	1.96E+01
HD 150680	364.5	11892480	3	3.335E+05	1.33E+03
HD 150706	110.2	5386240	3	6.656E+03	3.12E+01
HD 152222	96.9	7971584	3	5.203E+04	3.13E+02
	1136.3	20459520	3	5.187E+04	4.66E+01
	1136.3	20459776	10	5.142E+04	2.11E+01
HD 153458	387.1	5416704	3	2.799E+03	3.91E+01
HD 154391	96.9	7970560	3	3.023E+04	1.22E+02
HD 158460	96.9	7970048	3	7.931E+03	5.71E+01
HD 158485	96.9	7969280	3	3.564E+03	2.80E+01
HD 159048	96.9	7970816	3	3.600E+04	1.88E+02
HD 159222	320.9	5436672	3	9.997E+03	2.90E+01
	634.1	13590016	3	9.787E+03	5.20E+01
	1134.3	20462080	3	1.019E+04	4.86E+01
	1134.3	20462336	10	9.952E+03	2.10E+01
	1134.3	20462592	30	1.020E+04	1.36E+01
HD 159330	42.5	6941696	3	7.978E+04	2.77E+02
	49.5	7143424	3	7.977E+04	3.18E+02
	49.5	7143680	3	7.957E+04	3.26E+02
	49.6	7143936	3	7.953E+04	3.27E+02
	49.6	7144192	3	7.934E+04	3.20E+02
	49.6	7144448	3	7.936E+04	3.06E+02
	53.8	7166976	3	8.024E+04	2.92E+02
	60.9	7200512	3	7.975E+04	2.96E+02
	61.4	7202048	3	8.030E+04	2.86E+02
	70.7	7337728	3	7.946E+04	2.95E+02
	69.4	7346688	3	7.951E+04	4.85E+02
	69.0	7348736	3	7.933E+04	2.79E+02
	73.4	7428608	3	7.980E+04	2.98E+02
	73.4	7430144	10	8.084E+04	3.96E+02
	58.8	7640320	3	7.979E+04	2.96E+02
	69.8	7744256	3	7.967E+04	2.97E+02
	90.6	7795712	3	7.915E+04	2.96E+02
	96.5	7974400	3	7.913E+04	2.87E+02
	84.1	7978752	3	7.963E+04	2.96E+02
	84.1	7980544	3	7.959E+04	2.94E+02
	104.8	8137216	3	7.927E+04	2.90E+02
	106.8	8137984	3	7.995E+04	3.03E+02
	107.9	8342016	3	7.977E+04	2.96E+02
	125.8	8379904	3	7.914E+04	2.91E+02
	127.2	8380672	3	7.958E+04	2.82E+02
	109.9	8782592	3	7.947E+04	2.84E+02
	153.5	8809472	3	7.964E+04	3.04E+02
	157.0	8819200	3	7.977E+04	2.99E+02
	162.1	8937472	3	7.979E+04	2.90E+02
	178.8	9066496	3	7.905E+04	2.90E+02
	182.2	9066752	3	7.926E+04	2.98E+02
	185.1	9181440	3	7.952E+04	3.00E+02
	201.7	9190912	3	7.900E+04	2.88E+02

TABLE 2 (*Continued*)

Name	Days Since Mission Start	AOR Key[a]	DCE[b] Time (s)	Count Rate (DN s^{-1})	Uncertainty (DN s^{-1})
	205.6	9221632	3	7.964E+04	3.01E+02
	209.5	9222400	3	7.960E+04	3.10E+02
	224.7	9457408	3	7.913E+04	3.00E+02
	231.9	9617664	3	7.928E+04	3.09E+02
	228.9	9640192	3	7.915E+04	3.16E+02
	250.7	9658368	3	7.918E+04	3.11E+02
	253.5	9658880	3	7.932E+04	3.02E+02
	258.0	9659392	3	7.937E+04	3.02E+02
	276.9	9802496	3	7.919E+04	3.11E+02
	281.7	9803264	3	7.919E+04	3.03E+02
	284.5	9804032	3	7.939E+04	3.17E+02
	298.2	9937152	3	7.898E+04	3.08E+02
	300.6	9938688	3	7.924E+04	3.19E+02
	303.5	9939456	3	7.910E+04	3.11E+02
	317.6	10087936	3	7.891E+04	2.99E+02
	319.7	10088704	3	7.931E+04	3.21E+02
	322.5	10089472	3	7.911E+04	3.08E+02
	338.6	11780352	3	7.878E+04	2.98E+02
	342.1	11781120	3	7.929E+04	3.11E+02
	345.1	11781888	3	7.969E+04	3.04E+02
	347.4	11782656	3	7.914E+04	2.95E+02
	359.7	11891200	3	7.911E+04	3.04E+02
	362.6	11897088	3	7.930E+04	3.11E+02
	368.0	11897856	3	7.930E+04	3.04E+02
	385.6	12060160	3	7.883E+04	2.99E+02
	389.5	12060928	3	7.921E+04	3.07E+02
	393.0	12061696	3	7.947E+04	2.98E+02
	397.8	12152832	3	7.941E+04	3.00E+02
	414.5	12194560	3	7.885E+04	2.85E+02
	418.0	12195328	3	7.875E+04	3.06E+02
	421.5	12196096	3	7.921E+04	2.99E+02
	438.8	12394496	3	7.934E+04	2.96E+02
	434.5	12395264	3	7.917E+04	2.96E+02
	443.4	12396032	3	7.952E+04	3.02E+02
	516.6	13108992	3	7.879E+04	2.88E+02
	529.4	13110016	3	7.901E+04	2.99E+02
	521.7	13111040	3	7.887E+04	3.04E+02
	550.6	13295360	3	7.862E+04	2.90E+02
	557.8	13298176	3	7.933E+04	3.03E+02
	563.1	13299200	3	7.904E+04	3.02E+02
	584.5	13428992	3	7.880E+04	2.96E+02
	591.0	13431552	3	7.863E+04	2.97E+02
	596.6	13432320	3	7.905E+04	3.13E+02
	634.3	13585408	3	7.937E+04	3.14E+02
	624.6	13586176	3	7.866E+04	2.98E+02
	629.4	13586944	3	7.908E+04	3.02E+02
	634.4	13587712	3	7.944E+04	3.08E+02
	660.6	15217152	3	7.896E+04	3.01E+02
	667.8	15220480	3	7.917E+04	3.14E+02
	701.5	15413248	3	7.889E+04	3.00E+02
	704.9	15414272	3	7.898E+04	3.10E+02
	709.3	15415296	3	7.920E+04	3.09E+02
	731.6	15815168	3	7.899E+04	2.98E+02
	735.9	15816192	3	7.927E+04	3.04E+02
	742.1	15817216	3	7.919E+04	3.03E+02
	760.4	15991040	3	7.854E+04	3.04E+02
	767.9	16047616	3	7.916E+04	3.06E+02
	775.9	16048640	3	7.901E+04	2.95E+02
	800.4	16228608	3	7.868E+04	2.89E+02
	805.8	16254208	3	7.924E+04	3.00E+02
	810.8	16255232	3	7.925E+04	2.92E+02
	869.6	16603648	3	7.914E+04	2.92E+02
	872.1	16604416	3	7.909E+04	3.01E+02

TABLE 2 (*Continued*)

Name	Days Since Mission Start	AOR Key[a]	DCE[b] Time (s)	Count Rate (DN s^{-1})	Uncertainty (DN s^{-1})
	869.6	16619520	3	7.898E+04	2.96E+02
	904.0	16833792	3	7.899E+04	2.95E+02
	910.8	16834816	3	7.905E+04	2.91E+02
	921.2	16835840	3	7.883E+04	2.98E+02
	1134.3	20459008	3	7.921E+04	4.95E+01
	1134.3	20459264	10	7.932E+04	2.15E+01
HD 163466	96.9	7969024	3	2.952E+03	2.48E+01
	465.5	12872448	3	2.963E+03	3.71E+01
	630.4	13613824	3	2.841E+03	4.81E+01
HD 163588	97.0	7973376	3	4.503E+05	1.62E+03
	298.5	9942528	3	4.427E+05	2.42E+03
HD 165459	96.9	7968256	3	3.830E+03	3.82E+01
	283.0	9851392	3	3.853E+03	3.26E+01
HD 166780	96.9	7970304	3	3.072E+04	1.20E+02
	254.7	9660416	3	3.057E+04	1.30E+02
HD 167389	303.3	5434368	3	4.449E+03	2.66E+01
HD 170693	96.9	7971840	3	1.905E+05	6.87E+02
	905.8	16869888	3	1.877E+05	6.81E+02
	1136.3	20458496	3	1.830E+05	4.73E+01
	1136.3	20458752	10	1.861E+05	2.40E+01
HD 172066	96.9	7968512	3	3.368E+03	2.68E+01
HD 172728	96.9	7969792	3	4.754E+03	3.21E+01
	465.5	12872704	3	4.741E+03	3.04E+01
HD 173398	461.6	12871424	3	3.019E+04	1.21E+02
	466.6	12884224	3	3.050E+04	1.22E+02
	470.4	12884736	3	3.048E+04	1.26E+02
	484.6	12997120	3	3.014E+04	1.20E+02
	488.8	13001472	3	3.041E+04	1.24E+02
	496.4	13071872	10	3.082E+04	1.52E+02
	496.4	13072128	30	3.120E+04	1.52E+02
	496.5	13072640	3	3.030E+04	1.16E+02
	516.6	13108736	3	3.014E+04	1.15E+02
	529.4	13109760	3	3.016E+04	1.21E+02
	521.8	13110784	3	3.033E+04	1.23E+02
	550.5	13295104	3	3.013E+04	1.18E+02
	557.8	13297920	3	3.028E+04	1.22E+02
	563.0	13298944	3	3.020E+04	1.25E+02
	584.5	13428736	3	3.018E+04	1.22E+02
	591.0	13431296	3	3.016E+04	1.26E+02
	596.6	13432064	3	3.048E+04	1.32E+02
	634.3	13585152	3	3.043E+04	1.27E+02
	624.6	13585920	3	3.018E+04	1.24E+02
	629.4	13586688	3	3.026E+04	1.23E+02
	634.4	13587456	3	3.035E+04	1.28E+02
	660.6	15216896	3	3.006E+04	1.24E+02
	667.8	15220224	3	3.036E+04	1.26E+02
	674.2	15221248	3	3.043E+04	1.29E+02
	701.5	15412992	3	3.022E+04	1.23E+02
	704.9	15414016	3	3.036E+04	1.25E+02
	709.3	15415040	3	3.047E+04	1.29E+02
	731.6	15814912	3	3.030E+04	1.21E+02
	735.9	15815936	3	3.031E+04	1.26E+02
	742.1	15816960	3	3.040E+04	1.28E+02
	760.4	15990784	3	3.000E+04	1.21E+02
	767.9	16047360	3	3.034E+04	1.27E+02
	775.9	16048384	3	3.023E+04	1.25E+02
	800.4	16228352	3	3.009E+04	1.22E+02
	805.8	16253952	3	3.076E+04	1.28E+02
	810.8	16254976	3	3.035E+04	1.19E+02
	827.8	16374528	3	3.000E+04	1.17E+02
	830.8	16375296	3	3.030E+04	1.22E+02
	835.9	16376832	3	3.031E+04	1.21E+02
	864.7	16602624	3	3.008E+04	1.18E+02

TABLE 2 (*Continued*)

Name	Days Since Mission Start	AOR Key[a]	DCE[b] Time (s)	Count Rate (DN s^{-1})	Uncertainty (DN s^{-1})
	869.6	16603392	3	3.043E+04	1.19E+02
	872.0	16604160	3	3.045E+04	1.23E+02
	904.0	16833536	3	3.037E+04	1.20E+02
	910.8	16834560	3	3.030E+04	2.03E+02
	921.2	16835584	3	3.040E+04	1.25E+02
	905.8	16870144	3	3.025E+04	1.28E+02
HD 173511	96.9	7971072	3	3.165E+04	1.24E+02
HD 173976	96.9	7971328	3	4.749E+04	1.72E+02
HD 174123	96.9	7968000	3	2.296E+03	2.39E+01
HD 176841	96.9	7968768	3	3.644E+03	2.79E+01
HD 180711	97.0	7973632	3	5.796E+05	2.09E+03
	280.7	9805568	3	5.722E+05	2.07E+03
HD 183439	70.7	7334144	3	7.201E+05	3.67E+03
	70.8	7335424	3	7.198E+05	3.81E+03
HD 189276	97.0	7973120	3	3.868E+05	1.38E+03
	280.7	9805824	3	3.844E+05	1.51E+03
HD 191854	96.9	7969536	3	5.075E+03	4.82E+01
	254.7	9660672	3	4.652E+03	3.60E+01
	254.7	9661184	10	4.922E+03	2.69E+01
HD 193017	415.0	5410560	3	4.150E+03	3.86E+01
HD 195034	439.3	5426688	3	6.127E+03	3.33E+01
HD 199598	301.8	5413632	3	7.021E+03	3.60E+01
HD 201941	280.7	9806080	3	2.900E+03	2.79E+01
HD 204277	435.3	5374976	3	7.301E+03	2.83E+01
HD 205905	417.6	5405440	3	7.871E+03	3.42E+01
HD 209952	69.4	7345152	3	1.468E+05	5.43E+02
	84.0	7979008	3	1.462E+05	5.16E+02
HD 212291	441.9	5421312	3	3.319E+03	3.19E+01
HD 216131	96.9	7972608	3	3.277E+05	1.24E+03
HD 216275	318.5	5435136	3	5.062E+03	4.07E+01
HD 217382	97.0	7972864	3	3.264E+05	1.18E+03
NPM1 +61.0569	465.5	12872960	3	1.510E+03	1.64E+01
NPM1 +68.0412	415.5	12196864	3	1.494E+03	1.67E+01
SAO 9310	415.5	12197120	3	1.069E+03	1.24E+01

[a] The "AOR key," or astronomical observation request key, is used by the *Spitzer* Science Center to uniquely identify the observation.

[b] "DCE" refers to "data collection event," in this case an individual image.

measurements throughout the MIPS dynamic range, so we must incorporate additional data sets into our flux predictions for the bright 24 μm calibrators. We discuss here the validation of additional data sets and derive the scale factors required to put them on the same system as the 2MASS read-1 measurements (and therefore the same system as the MIPS 24 μm measurements), allowing direct comparison to the results of G. H. Rieke et al. (2007, in preparation).

4.1.1. 2MASS Saturated-Source Magnitudes

Below magnitudes of ~4.5, 4, and 3.5 at *J*, *H*, and K_s, respectively, 2MASS data are saturated even in the read-1 measurements used to constrain the calibration factor derived in § 3. Measurements for saturated sources are reported by the 2MASS project and are obtained by fitting to the radial profiles of the unsaturated portion of the stellar image, but large uncertainties of 20%–30% are associated with these measurements. To reduce the uncertainties associated with using the saturated 2MASS magnitudes, we compute the offset between the saturated and read-1 magnitudes.

Kimeswenger (2005) presents photometry in the *J* and K_s bands for a sample of ~600 stars that overlaps the 2MASS read-1 and saturated-source magnitude ranges. This bright-star survey uses the same camera as the Deep Near-Infrared Survey of the Southern Sky (DENIS) with the addition of neutral-density filters, so we apply the DENIS transformations computed by Carpenter (2001) to put the magnitudes on the 2MASS system. (This step is not strictly necessary, since, as we discuss below, we are using these measurements differentially.) We compare the 2MASS measurements to those by Kimeswenger (2005) over different magnitude ranges to determine the offset between the 2MASS read-1 and saturated-source magnitudes. At faint levels (well above the limits quoted above, to ensure that read-1 measurements were not affected by any saturated sources), the 2MASS and the transformed Kimeswenger (2005) magnitudes are in excellent agreement: the weight-

TABLE 3
DATA USED TO COMPUTE THE 24 μm CALIBRATION FACTOR

Name	K_s[a] (mag)	24 μm Count Rate (DN s^{-1})	Uncertainty (DN s^{-1})	Calibration Factor (MJy sr^{-1} [DN s^{-1}]$^{-1}$)	Uncertainty (MJy sr^{-1} [DN s^{-1}]$^{-1}$)
HD 000319	5.479	6.708E+03	5.00E+01	4.513E−02	1.39E−03
HD 002811	7.057	1.591E+03	3.35E+01	4.448E−02	1.63E−03
HD 011413	5.422	7.866E+03	3.87E+01	4.056E−02	1.23E−03
HD 014943	5.439	7.180E+03	2.84E+01	4.374E−02	1.32E−03
HD 015646	6.411	2.997E+03	4.85E+01	4.281E−02	1.46E−03
HD 017254	5.877	4.529E+03	1.97E+01	4.632E−02	1.40E−03
HD 020888	5.691	5.519E+03	2.04E+01	4.512E−02	1.36E−03
HD 021981	5.526	6.089E+03	1.33E+01	4.761E−02	1.43E−03
HD 034868	6.024	3.851E+03	3.89E+01	4.758E−02	1.51E−03
HD 042525	5.751	5.116E+03	2.85E+01	4.606E−02	1.40E−03
HD 057336	7.114	1.403E+03	3.44E+01	4.786E−02	1.86E−03
HD 073210	6.165	3.707E+03	5.55E+01	4.341E−02	1.45E−03
HD 073666	6.532	2.541E+03	5.66E+01	4.517E−02	1.69E−03
HD 073819	6.280	3.170E+03	5.29E+01	4.566E−02	1.57E−03
HD 092845	5.513	7.166E+03	4.51E+01	4.094E−02	1.26E−03
HD 101452	6.819	1.910E+03	3.50E+01	4.613E−02	1.62E−03
HD 105805	5.600	5.734E+03	5.10E+01	4.722E−02	1.48E−03
HD 116706	5.502	6.188E+03	5.01E+01	4.789E−02	1.49E−03
HD 128998	5.756	4.824E+03	2.79E+01	4.862E−02	1.48E−03
HD 158485	6.145	3.564E+03	2.79E+01	4.599E−02	1.43E−03
HD 163466	6.339	2.917E+03	2.94E+01	4.699E−02	1.49E−03
HD 172728	5.753	4.747E+03	2.21E+01	4.954E−02	1.50E−03

NOTE.—The average calibration factor is 4.54×10^{-2} MJy sr^{-1} (DN s^{-1})$^{-1}$, to which we have assigned an uncertainty of 2% (see § 3).

[a] K_s = [24] for the stars in this table (see G. H. Rieke et al. 2007, in preparation), all of which are between types A0 and A6.

ed average (rejecting points more than 3 σ from the median) of J(2MASS) − J(Kimeswenger) between magnitudes 8.5 and 5.6 is 0.001 ± 0.002 mag, and K_s(2MASS) − K_s(Kimeswenger) between magnitudes 7.5 and 4.2 is 0.023 ± 0.003 mag. Below those magnitude limits, the offsets are J(2MASS) − J(Kimeswenger) = 0.053 ± 0.005 mag and K_s(2MASS) − K_s(Kimeswenger) = 0.058 ± 0.008 mag. The difference between the faint J magnitudes is not significant, but we do include the difference between the faint K_s magnitudes in computing offsets ($m_{\rm read\text{-}1} - m_{\rm sat}$) of −0.053 mag at J and −0.035 mag at K_s. These offsets are added to saturated 2MASS magnitudes to put them on the read-1 scale. To further reduce the uncertainty, we average the J and K_s magnitudes to compute a "super"-K_s magnitude, after correcting J to K_s using the $J - K$ colors (after correcting the colors to the 2MASS system using the transformations computed by Carpenter 2001) of stars tabulated by Tokunaga (2000).

4.1.2. Johnson Photometry

Johnson et al. (1966) measured ~650 bright stars in the J and K bands. This sample is large and homogeneously observed, and the measurements have significantly smaller uncertainties than the saturated sources observed by 2MASS. For example, the star HD 001013 was observed 91 times by Johnson et al. (1966). After applying an air mass correction derived from the data, we find a rms deviation of 0.037 mag in these measurements. We conservatively assign a 1 σ uncertainty of 0.04 mag to the photometry by Johnson et al. (1966).

To compute the offset between the Johnson et al. (1966) magnitudes and 2MASS, we transform the measurements to the 2MASS system using the equations derived by Carpenter (2001) for the Koornneef (1983) system, which is most similar to the system used by Johnson et al. (1966). The weighted average (rejecting points more than 3 σ from the median) of J(2MASS) − J(transformed Johnson) is 0.028 ± 0.007 mag and of K_s(2MASS) − K(transformed Johnson) is 0.004 ± 0.005 mag. The offset in the K_s band is not significant, but we apply a correction of 0.028 mag to the measurements at J. In addition, since all the MIPS calibrators that were also measured by Johnson et al. (1966) are well into the saturated 2MASS range, we apply the same offsets applied to the saturated 2MASS measurements, for net corrections of −0.025 mag at J and −0.035 mag at K_s (plus the color transformation from Johnson to 2MASS). Finally, we combine the J and K_s data to form super-K_s as for the 2MASS data.

4.1.3. IRAS Measurements

Many of the bright MIPS calibrators were detected by *IRAS* at 12 and 25 μm. The MIPS 24 μm band was demonstrated by G. H. Rieke et al. (2007, in preparation) to be linear within ~1% below 1 Jy, so we can use the overlap between MIPS and *IRAS* measurements in this flux range to constrain the

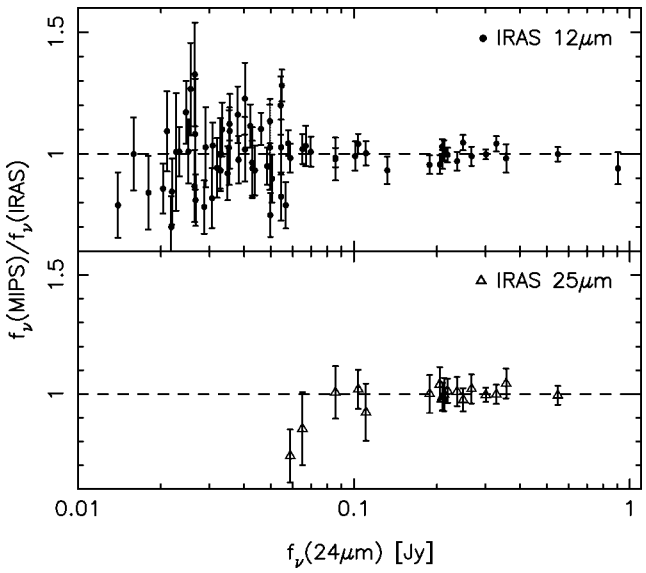

FIG. 5.—Ratio of MIPS 24 μm flux densities to *IRAS* 12 and 25 μm flux densities (*filled circles and open triangles, respectively*) as a function of 24 μm flux density, normalized to the average ratios of 0.265 and 1.11, respectively. The error bars represent the combined *IRAS* and MIPS uncertainties. A dashed line is drawn at a ratio of 1 as a guide.

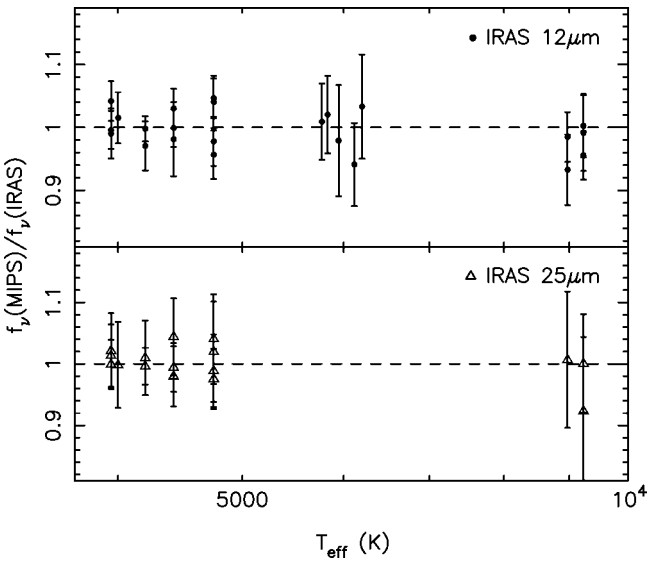

FIG. 6.—Ratio of MIPS 24 μm flux densities to *IRAS* 12 and 25 μm flux densities (*filled circles and open triangles, respectively*) as a function of spectral type, here quantified as the effective temperature of the star. The ratios have been normalized to the average ratios at 0.265 and 1.11 at 12 and 25 μm. The error bars represent the combined *IRAS* and MIPS uncertainties. A dashed line is drawn at a ratio of 1 as a guide.

linearity of *IRAS* and probe for effects of molecular absorptions in the 12 μm band. To ensure that the *IRAS* measurements are on the same scale as the other photometry that we use to predict flux densities for our calibrators, we empirically derive the ratio between the *IRAS* bands and the MIPS 24 μm band below 1 Jy for the calibrator stars, then apply this result over the full range of calibrator fluxes.

We obtain *IRAS* measurements of the MIPS calibrators from the faint-source catalog (FSC; used because the improved sensitivity relative to the point-source catalog provides more overlap with the MIPS sample), using only high-quality (quality flag "3") measurements. We applied color corrections appropriate to the temperature of each star to these observations and also applied the corrections measured by G. H. Rieke et al. (2007, in preparation): 0.992 at 12 μm and 0.980 at 25 μm. The ratio of the MIPS 24 μm measurement to the *IRAS* measurement, normalized to the average ratio, is plotted in Figure 5. The scatter in the measurements becomes obviously larger near the *IRAS* detection limit, around the equivalent 24 μm flux density of 60 and 80 mJy at 12 and 25 μm, respectively. The slope of the ratio as a function of brightness above these limits is consistent with 0 for both bands, indicating that they are linear in this brightness range. The average value of $f_\nu(24\ \mu\text{m})/f_\nu(12\ \mu\text{m})$ is 0.265, while $f_\nu(24\ \mu\text{m})/f_\nu(25\ \mu\text{m})$ is 1.11. Both values are very similar to the values derived from Kurucz (1993) models of these stars, 0.266 and 1.11, respectively. As shown in Figure 6, $f_\nu(24\ \mu\text{m})/f_\nu(12\ \mu\text{m})$ has a mild dependence on temperature (possibly the result of molecular absorptions in the 12 μm band becoming important in cool stars), so the ratio is better described as $0.276 - 1.94 \times 10^{-6} T_{\rm eff}[\text{K}]$. No significant trend with temperature is detected at 25 μm. The factors that we derive in this section to convert the zero points of saturated 2MASS magnitudes, Johnson et al. (1966) magnitudes, and *IRAS* 12 and 25 μm measurements to the system used by MIPS are summarized in Table 4.

4.2. The Calibration of Cool Stars

We compute an average super-$K_s - [24]$ (by applying the aperture correction, 1.08, derived in § 2.4 and the calibration factor derived in § 3 to the measurements in Table 2) color for the cool (K and M giants) stars in our sample, which can be compared directly to the A and G star color computed by G. H. Rieke et al. (2007, in preparation) modulo any offset (typically a fraction of a percent) between super-K_s and K_s. The weighted average color of the K and M stars in our sample

TABLE 4
ZERO-POINT CONVERSIONS

Data Set	Conversion Factor
2MASS saturated J	−0.053 mag
2MASS saturated K_s	−0.035 mag
Johnson J	−0.025 mag
Johnson K	−0.035 mag
IRAS 12 μm	× 0.266
IRAS 25 μm	× 1.11

NOTE.—These factors convert measurements to 24 μm magnitudes (NIR) or fluxes (*IRAS*; see § 4.1).

(after rejecting points greater than 3 σ from the mean) is 0.104 ± 0.006 mag.

4.3. Predictions

We list the photometry used to constrain the flux density predictions, after applying the corrections detailed above, in Table 5. The 24 μm flux densities for each source are the weighted average of the predictions derived from the entries in that table. We also list the predicted flux densities and their uncertainties in Table 5. We note that the predictions can be slightly different than those implicit in Table 3, since we used super-K_s in Table 5 and K_s was used in Table 3, although the average difference is insignificant: 0.002 ± 0.005 mag. We also include predicted background levels, computed using the *Spitzer* Planning Observations Tool[7] (SPOT); the background listed is the average of the range when the target is visible, and the uncertainty is half the difference between the extreme values.

5. CHECKS ON THE 24 μm CALIBRATION

In this section, we perform various checks on the 24 μm calibration, such as repeatability, linearity, and the effects of spectral type, exposure time, and background. Except for the repeatability check, we compute a single calibration factor for each star by dividing the prediction (Table 5) by the pixel area and the weighted average of all measurements of the count rate for each star (Table 6). The calibration factors derived from some stars differ from the adopted calibration factor by more than 5 σ; these stars were not used in the checks below. As shown in Table 7, most of the rejected stars show infrared fluxes above the predictions (i.e., the calibration factor is low).

5.1. Repeatability

The primary routine calibrator for the MIPS 24 μm channel is HD 159330, a K2 III star near the *Spitzer* continuous viewing zone (CVZ). When visible, this star is observed each time the instrument is turned on, to monitor photometric stability and check for changes in the calibration. A second routine calibrator, the K0 III star HD 173398, is also monitored to fill in the gaps when HD 159330 is not visible. We plot 100 measurements of HD 159330 and 46 measurements of HD 173398 in Figure 7. The rms scatter in the HD 159330 measurements is 0.4% (compared to 0.7% in the SSC pipeline–reduced data discussed in § 2.5), while the scatter in the HD 173398 measurements is 0.5%. A gradual reduction in the instrument response of ~0.5% over the first 300 days is apparent in the data and is the cause of some of the scatter computed for HD 159330. As this trend is insignificant compared to the uncertainty on the absolute calibration (cf. § 3), we have not attempted to correct it.

[7] See http://ssc.spitzer.caltech.edu/propkit/spot/.

5.2. Linearity

We check for effects of flux nonlinearity in the calibration by comparing calibration factors over a range of 460 in source brightness. We plot the calibration factors in Figure 8. We find no significant trend of calibration factor with source brightness—a least-squares fit to the data shows a difference of only 0.3% between 9 mJy and 4 Jy. The observed scatter of calibration factors is larger than can be explained by the error bars. The unaccounted-for scatter in the calibration factors is likely due to systematic uncertainties on the flux predictions for the individual stars, possibly from variability or small infrared excesses.

5.3. Spectral Type

As discussed in § 4, we have derived calibration factors using three broad types of stars (hot dwarfs, solar analogs, and cool giants) to look for systematic effects with stellar temperature. The weighted average calibration factor of each broad spectral type is 4.49×10^{-2}, 4.62×10^{-2}, and 4.49×10^{-2} MJy sr^{-1} (DN s^{-1})$^{-1}$ for 32 A, 37 G, and 25 K/M stars, respectively. These values are all consistent with the adopted calibration factor within the uncertainty (deviating by -1.1%, 1.8%, and -1.1%, respectively), but the differences may reflect real uncertainties in the colors of different types of stars and in our treatment of saturated 2MASS magnitudes.

5.4. Exposure Time

A small subset of the calibrators (11 stars) was measured using 10 and 30 s exposures in addition to the 3 s exposures—the weighted average counts per second from these stars is 1% and 2% higher using 10 and 30 s exposures, respectively. We find that the residual images in the 10 and 30 s exposures are roughly twice as bright as in the 3 s exposures, so it is likely that the excess is due to buildup of residual charge during the longer exposures.

5.5. Background

In general, astronomical sources of interest at 24 μm will be observed against a wide range of background levels, so we examine whether the derived calibration factor depends on background. Such an effect might be expected due to background light scattering onto the detector or due to systematic effects on the droop correction. We find no significant effect on the calibration over a factor of ~5 in background, as shown in Figure 9. A least-squares fit to the data indicates a slope of only marginal significance: $5.4 \times 10^{-4} \pm 2.9 \times 10^{-4}$ MJy sr^{-1} (DN s^{-1})$^{-1}$ (MJy sr^{-1})$^{-1}$.

5.6. Comparison to Another Infrared Calibration

As discussed in detail by G. H. Rieke et al. (2007, in preparation) and cited in § 4.1.3, the calibration presented here is based on an updated calibration system that is offset by a small

TABLE 5
MIPS Stellar Flux Calibrator Sample

Name	Spectral Type	Super-K_s[a] (mag)	Unc. (mag)	$f_\nu(12\ \mu m)$[b] (Jy)	Unc. (Jy)	$f_\nu(25\ \mu m)$[b] (Jy)	Unc. (Jy)	Predictions $f_\nu(24\ \mu m)$[c] (Jy)	Unc. (Jy)	$bkgd_{24}$[d] (MJy sr^{-1})	Unc. (MJy sr^{-1})
BD +621644	K5	5.258	0.013	…	…	…	…	6.355E−02	1.50E−03	1.54E+01	2.38E+00
HD 000319	A1 V	5.541	0.014	…	…	…	…	4.356E−02	1.14E−03	3.43E+01	6.33E+00
HD 001160	A0	7.020	0.018	…	…	…	…	1.116E−02	3.17E−04	4.92E+01	1.34E+01
HD 001644	K0 III	5.370	0.016	2.700E−01	3.24E−02	…	…	5.659E−02	1.52E−03	4.99E+01	1.37E+01
HD 001753	F5 V	7.730	0.017	…	…	…	…	6.047E−03	1.83E−04	1.81E+01	2.37E+00
HD 002151	G2 IV	1.307	0.193	8.471E+00	3.39E−01	2.099E+00	1.05E−01	2.279E+00	7.22E−02	1.72E+01	2.59E+00
HD 002261	K0 III	−0.143	0.223	3.866E+01	2.71E+00	9.149E+00	6.40E−01	1.010E+01	4.95E−01	2.27E+01	2.91E+00
HD 002811	A3 V	7.086	0.017	…	…	…	…	1.050E−02	2.92E−04	2.21E+01	2.73E+00
HD 003712	K0 IIIa	−0.308	0.028	…	…	…	…	1.048E+01	3.75E−01	1.97E+01	3.90E+00
HD 004128	K0 III	−0.323	0.028	4.320E+01	2.59E+00	9.303E+00	5.58E−01	1.070E+01	2.95E−01	3.45E+01	5.88E+00
HD 006860	M0 III	−1.897	0.028	2.000E+02	1.40E+01	4.618E+01	3.23E+00	4.711E+01	1.38E+00	2.75E+01	6.10E+00
HD 008941	F8 V	5.356	0.014	2.500E−01	3.00E−02	…	…	5.430E−02	1.52E−03	4.51E+01	1.22E+01
HD 009053	M0 IIIa	−0.480	0.204	5.187E+01	2.59E+00	1.178E+01	5.89E−01	1.329E+01	4.75E−01	2.03E+01	1.68E+00
HD 009927	K3 III	0.681	0.028	1.618E+01	8.09E−01	3.651E+00	1.83E−01	4.181E+00	1.07E−01	2.31E+01	5.07E+00
HD 011413	A1 V	5.484	0.013	1.993E−01	2.19E−02	…	…	4.622E−02	1.15E−03	1.85E+01	1.16E+00
HD 012533	K3 IIb	−0.824	0.028	6.979E+01	3.49E+00	1.672E+01	8.36E−01	1.756E+01	4.48E−01	2.69E+01	6.32E+00
HD 012929	K2 III	−0.715	0.028	5.904E+01	2.95E+00	1.401E+01	8.40E−01	1.537E+01	4.06E−01	4.24E+01	1.16E+01
HD 014943	A5 V	5.481	0.018	1.647E−01	1.32E−02	…	…	4.586E−02	1.23E−03	1.77E+01	8.12E−01
HD 015008	A1/2 V	3.995	0.124	7.404E−01	2.96E−02	1.696E−01	1.36E−02	1.971E−01	6.92E−03	1.62E+01	2.00E+00
HD 015646	A0 V	6.394	0.015	…	…	…	…	1.986E−02	5.29E−04	1.64E+01	1.76E+00
HD 017254	A2 V	5.923	0.013	1.275E−01	1.66E−02	…	…	3.076E−02	7.72E−04	1.73E+01	8.88E−01
HD 017709	K5 III	0.727	0.028	1.624E+01	8.12E−01	3.946E+00	2.37E−01	4.152E+00	1.10E−01	3.48E+01	9.17E+00
HD 018884	M1.5 III	−1.730	0.028	1.634E+02	6.54E+00	3.954E+01	1.98E+00	4.100E+01	9.82E−01	4.26E+01	9.55E+00
HD 019019	F8	5.563	0.017	1.714E−01	2.06E−02	…	…	4.456E−02	1.31E−03	4.45E+01	1.04E+01
HD 020644	K4 III	0.807	0.158	1.494E+01	7.47E−01	3.502E+00	1.75E−01	3.895E+00	1.38E−01	4.39E+01	1.22E+01
HD 020722	K3.5 III	6.010	0.015	1.234E−01	1.48E−02	…	…	3.118E−02	8.17E−04	1.81E+01	1.01E+00
HD 020888	A3 V	5.722	0.017	1.471E−01	1.47E−02	…	…	3.706E−02	9.94E−04	1.59E+01	1.99E+00
HD 020902	F5 I	0.490	0.028	…	…	…	…	4.566E+00	1.63E−01	2.70E+01	6.37E+00
HD 021981	A1 V	5.590	0.019	1.421E−01	1.14E−02	…	…	4.126E−02	1.13E−03	1.69E+01	9.66E−01
HD 022686	A0	7.154	0.015	…	…	…	…	9.861E−03	2.63E−04	3.86E+01	8.43E+00
HD 024512	M2 III	−1.003	0.244	8.013E+01	3.21E+00	1.972E+01	7.89E−01	2.136E+01	6.24E−01	1.59E+01	2.26E+00
HD 025025	M1 IIIb	−1.022	0.028	7.756E+01	3.88E+00	1.917E+01	9.59E−01	2.048E+01	5.22E−01	2.58E+01	4.15E+00
HD 025860	A4/5 IV	6.112	0.014	1.064E−01	1.70E−02	…	…	2.581E−02	6.65E−04	1.64E+01	1.39E+00
HD 027466	G5	6.274	0.014	1.170E−01	2.11E−02	…	…	2.323E−02	6.59E−04	3.03E+01	6.02E+00
HD 028099	G2 V	6.547	0.016	…	…	…	…	1.798E−02	5.35E−04	5.00E+01	1.30E+01
HD 028471	G5 V	6.323	0.017	9.760E−02	1.56E−02	…	…	2.219E−02	6.61E−04	1.54E+01	1.90E+00
HD 029139	K5 III	−2.868	0.028	4.468E+02	2.23E+01	1.059E+02	6.36E+00	1.135E+02	3.00E+00	4.98E+01	1.29E+01
HD 029461	G5 V	6.436	0.021	…	…	…	…	1.991E−02	6.51E−04	4.79E+01	1.22E+01
HD 030246	G5 V	6.725	0.021	…	…	…	…	1.526E−02	4.99E−04	4.83E+01	1.26E+01
HD 031398	K3 II	−0.607	0.028	…	…	…	…	1.380E+01	4.94E−01	4.52E+01	1.25E+01
HD 032384	G5 V	7.121	0.015	…	…	…	…	1.060E−02	3.10E−04	1.53E+01	2.06E+00
HD 032831	K3 III	1.721	0.028	5.984E+00	1.79E−01	1.408E+00	4.22E−02	1.581E+00	3.03E−02	1.79E+01	2.44E+00
HD 032887	K4 III	−0.285	0.028	3.936E+01	1.97E+00	9.121E+00	5.47E−01	1.025E+01	2.71E−01	2.10E+01	3.42E+00
HD 034029	G5 IIIE+	−1.898	0.028	…	…	…	…	4.532E+01	1.62E+00	3.29E+01	8.25E+00
HD 034377	G5 V	7.183	0.036	6.193E−02	1.05E−02	…	…	1.016E−02	4.34E−04	1.55E+01	1.97E+00
HD 034868	A0 V	6.014	0.019	9.262E−02	1.94E−02	…	…	2.811E−02	8.10E−04	1.95E+01	3.05E+00
HD 035666	K3 III	3.829	0.135	9.167E−01	3.67E−02	2.113E−01	1.27E−02	2.383E−01	7.88E−03	1.58E+01	2.32E+00
HD 036167	K5 III	0.772	0.205	…	…	3.309E+00	1.99E−01	3.688E+00	2.18E−01	3.19E+01	7.04E+00
HD 037962	G4 V	6.288	0.015	8.465E−02	2.03E−02	…	…	2.282E−02	6.62E−04	1.85E+01	3.01E+00
HD 038921	A0 V	7.521	0.014	…	…	…	…	7.033E−03	1.84E−04	1.74E+01	2.64E+00
HD 038944	M0 III	0.634	0.028	…	…	…	…	4.401E+00	1.58E−01	4.16E+01	1.12E+01
HD 038949	G1 V	6.424	0.018	…	…	…	…	2.013E−02	6.22E−04	2.00E+01	3.57E+00
HD 039425	K2 III	0.444	0.028	2.030E+01	1.01E+00	4.530E+00	2.27E−01	5.210E+00	1.33E−01	1.78E+01	2.73E+00
HD 039608	K5 III	3.803	0.120	1.014E+00	4.06E−02	2.358E−01	1.41E−02	2.621E−01	8.61E−03	1.55E+01	2.14E+00
HD 040129	G5 V	6.807	0.016	6.654E−02	1.13E−02	…	…	1.422E−02	4.17E−04	1.57E+01	1.77E+00
HD 040335	A1 II	6.434	0.015	…	…	…	…	1.914E−02	5.10E−04	3.45E+01	8.00E+00
HD 041371	K0 III	4.742	0.019	3.750E−01	1.50E−02	9.177E−02	7.34E−03	9.982E−02	2.28E−03	1.55E+01	2.22E+00
HD 042525	A0 V	5.768	0.016	1.186E−01	7.12E−03	…	…	3.477E−02	8.64E−04	1.55E+01	2.26E+00
HD 042701	K3 III	3.595	0.217	1.134E+00	2.27E−02	2.724E−01	8.17E−03	2.990E−01	5.41E−03	1.55E+01	2.28E+00
HD 043107	B8 V	5.197	0.013	2.085E−01	1.04E−02	…	…	5.942E−02	1.36E−03	1.55E+01	2.31E+00

TABLE 5 (*Continued*)

Name	Spectral Type	Super-K_s[a] (mag)	Unc. (mag)	$f_\nu(12\ \mu m)$[b] (Jy)	Unc. (Jy)	$f_\nu(25\ \mu m)$[b] (Jy)	Unc. (Jy)	Predictions			
								$f_\nu(24\ \mu m)$[c] (Jy)	Unc. (Jy)	$bkgd_{24}$[d] (MJy sr^{-1})	Unc. (MJy sr^{-1})
HD 044431	G5 V	4.330	0.131	8.992E−01	2.70E−02	2.372E−01	9.49E−03	2.355E−01	5.87E−03	1.66E+01	2.73E+00
HD 044594	G3 V	5.119	0.019	2.399E−01	1.44E−02	6.873E−02	1.24E−02	6.641E−02	1.83E−03	1.63E+01	2.40E+00
HD 045348	F0 II	−1.403	0.028	1.064E+02	3.19E+00	2.524E+01	7.57E−01	2.763E+01	5.29E−01	1.62E+01	2.19E+00
HD 045557	A0 V	5.763	0.012	1.230E−01	1.23E−02	…	…	3.538E−02	8.61E−04	1.56E+01	2.31E+00
HD 046190	A0 V	6.396	0.015	7.604E−02	1.14E−02	…	…	1.985E−02	5.21E−04	1.56E+01	2.33E+00
HD 046819	K0 III	5.302	0.015	2.249E−01	1.35E−02	7.168E−02	1.08E−02	5.996E−02	1.45E−03	1.55E+01	2.36E+00
HD 047332	A1 IV	6.687	0.013	8.042E−02	1.45E−02	…	…	1.523E−02	3.86E−04	1.59E+01	2.61E+00
HD 048002	A5 IV	7.406	0.015	…	…	…	…	7.818E−03	2.08E−04	1.65E+01	2.38E+00
HD 048915	A0 V	−1.400	0.120	…	…	…	…	2.603E+01	3.18E+00	2.33E+01	4.84E+00
HD 050310	K1 III	0.335	0.200	2.312E+01	9.25E−01	5.862E+00	2.35E−01	6.265E+00	1.83E−01	1.66E+01	2.29E+00
HD 051799	M1 III	0.511	0.028	2.069E+01	8.28E−01	5.032E+00	2.01E−01	5.236E+00	1.19E−01	1.66E+01	2.40E+00
HD 053501	K3 III	2.084	0.202	4.718E+00	1.42E−01	1.180E+00	3.54E−02	1.269E+00	2.86E−02	1.57E+01	2.48E+00
HD 053811	A4 IV	4.665	0.127	3.976E−01	1.59E−02	9.668E−02	1.16E−02	1.067E−01	3.96E−03	1.66E+01	2.46E+00
HD 056413	G5 V	7.307	0.016	…	…	…	…	8.927E−03	2.66E−04	1.57E+01	2.65E+00
HD 056855	K3 Ib	−1.005	0.028	9.475E+01	3.79E+00	2.341E+01	9.37E−01	2.251E+01	5.16E−01	1.80E+01	3.34E+00
HD 057336	A0 IV	7.194	0.020	…	…	…	…	9.504E−03	2.83E−04	1.65E+01	2.72E+00
HD 057507	G5 V	7.114	0.018	…	…	…	…	1.066E−02	3.29E−04	1.56E+01	2.68E+00
HD 058142	A1 V	4.608	0.117	3.832E−01	2.30E−02	…	…	1.041E−01	5.62E−03	2.95E+01	6.98E+00
HD 059717	K5 III	−0.468	0.028	4.924E+01	2.46E+00	1.199E+01	5.99E−01	1.258E+01	3.21E−01	1.74E+01	2.83E+00
HD 060178	A2 V	1.431	0.028	7.211E+00	4.33E−01	1.624E+00	8.12E−02	1.893E+00	5.01E−02	4.50E+01	1.22E+01
HD 060522	M0 III	0.202	0.028	2.549E+01	1.27E+00	5.944E+00	2.38E−01	6.593E+00	1.59E−01	4.91E+01	1.33E+01
HD 061929	G5 V	6.366	0.014	7.234E−02	1.09E−02	…	…	2.115E−02	5.97E−04	1.55E+01	2.56E+00
HD 062509	K0 IIIb	−1.185	0.028	8.784E+01	3.51E+00	2.024E+01	1.01E+00	2.315E+01	5.54E−01	4.81E+01	1.30E+01
HD 064324	G0	6.242	0.013	…	…	…	…	2.381E−02	6.73E−04	4.16E+01	1.10E+01
HD 065517	A2/3 IV	6.879	0.019	…	…	…	…	1.270E−02	3.70E−04	1.66E+01	2.79E+00
HD 066751	F8	5.071	0.015	2.435E−01	1.95E−02	…	…	6.932E−02	1.91E−03	2.00E+01	3.84E+00
HD 069863	A2 V	4.954	0.014	3.275E−01	1.31E−02	7.684E−02	8.45E−03	7.822E−02	1.69E−03	1.55E+01	2.46E+00
HD 070272	K4.5 III	0.567	0.028	1.923E+01	9.62E−01	4.546E+00	2.27E−01	4.846E+00	1.24E−01	3.25E+01	7.63E+00
HD 071129	K3 III+	−1.696	0.119	1.723E+02	5.17E+00	4.329E+01	1.73E+00	4.563E+01	1.12E+00	1.58E+01	2.57E+00
HD 073210	A5 V	6.185	0.015	…	…	…	…	2.407E−02	6.42E−04	4.96E+01	1.31E+01
HD 073666	A1 V	6.516	0.015	…	…	…	…	1.775E−02	4.73E−04	4.95E+01	1.28E+01
HD 073819	A6 V	6.283	0.014	…	…	…	…	2.199E−02	5.74E−04	4.95E+01	1.29E+01
HD 075223	A1 V	7.279	0.026	…	…	…	…	8.789E−03	3.00E−04	2.00E+01	3.53E+00
HD 077281	A2	7.021	0.016	…	…	…	…	1.115E−02	3.03E−04	3.44E+01	9.28E+00
HD 080007	A2 IV	1.440	0.199	6.683E+00	2.67E−01	1.589E+00	6.36E−02	1.793E+00	5.22E−02	1.56E+01	2.61E+00
HD 080493	K7 III	−0.667	0.028	5.859E+01	2.93E+00	1.376E+01	8.26E−01	1.490E+01	3.94E−01	3.74E+01	8.71E+00
HD 081797	K3 II–III	−1.236	0.028	1.077E+02	6.46E+00	2.368E+01	1.42E+00	2.556E+01	7.06E−01	3.03E+01	7.64E+00
HD 082308	K5 III	0.567	0.028	2.031E+01	1.83E+00	4.486E+00	2.69E−01	4.798E+00	1.41E−01	4.76E+01	1.21E+01
HD 082621	A2 V	4.454	0.102	5.327E−01	3.20E−02	…	…	1.361E−01	7.16E−03	2.49E+01	4.74E+00
HD 082668	K5 III	−0.507	0.140	…	…	…	…	1.259E+01	1.78E+00	1.85E+01	2.60E+00
HD 087901	B7	1.508	0.028	6.272E+00	3.14E−01	1.466E+00	1.47E−01	1.765E+00	4.94E−02	4.97E+01	1.36E+01
HD 089388	K3 IIa	0.091	0.227	…	…	…	…	7.256E+00	1.66E+00	1.71E+01	2.68E+00
HD 089484	K1 IIIb	−0.705	0.028	6.156E+01	2.46E+00	1.378E+01	5.51E−01	1.547E+01	3.52E−01	4.68E+01	1.14E+01
HD 089758	M0 III	−0.967	0.028	7.416E+01	3.71E+00	1.775E+01	1.06E+00	1.936E+01	5.11E−01	2.85E+01	5.26E+00
HD 091056	M0 III	0.748	0.216	…	…	…	…	3.962E+00	8.60E−01	1.69E+01	2.77E+00
HD 091375	A1 V	4.696	0.320	4.151E−01	2.08E−02	1.081E−01	1.40E−02	1.134E−01	5.31E−03	1.62E+01	2.86E+00
HD 092305	M0 III	0.330	0.193	2.491E+01	9.97E−01	6.116E+00	3.06E−01	6.592E+00	2.09E−01	1.69E+01	2.95E+00
HD 092788	G5	5.733	0.023	…	…	…	…	3.805E−02	1.29E−03	4.22E+01	1.17E+01
HD 092845	A0 V	5.548	0.015	1.815E−01	3.08E−02	…	…	4.340E−02	1.14E−03	2.17E+01	4.09E+00
HD 093813	K0/K1 III	0.285	0.028	2.491E+01	1.49E+00	5.712E+00	4.00E−01	6.207E+00	1.76E−01	3.02E+01	6.93E+00
HD 095418	A1 V	2.248	0.028	3.320E+00	1.33E−01	9.755E−01	4.88E−02	9.326E−01	2.23E−02	2.12E+01	3.07E+00
HD 095578	M0 III	0.769	0.028	1.573E+01	1.10E+00	3.776E+00	2.27E−01	3.979E+00	1.13E−01	4.38E+01	1.22E+01
HD 095689	K0 Iab	−0.663	0.028	5.893E+01	2.36E+00	1.389E+01	6.94E−01	1.502E+01	3.59E−01	1.99E+01	2.80E+00
HD 096833	K1 III	0.389	0.028	2.111E+01	1.06E+00	5.086E+00	2.54E−01	5.556E+00	1.42E−01	2.49E+01	3.80E+00
HD 098230	F8.5 V	2.095	0.187	4.067E+00	2.03E−01	8.777E−01	5.27E−02	1.036E+00	3.98E−02	3.15E+01	5.38E+00
HD 098262	K3 III	0.269	0.028	2.457E+01	1.23E+00	5.808E+00	2.90E−01	6.296E+00	1.60E−01	3.05E+01	5.07E+00
HD 098553	G2.5 V	6.080	0.015	1.239E−01	1.61E−02	…	…	2.782E−02	7.94E−04	2.99E+01	6.51E+00
HD 100029	M0 III	−0.207	0.028	3.827E+01	1.53E+00	9.702E+00	4.85E−01	9.927E+00	2.38E−01	1.81E+01	2.53E+00
HD 100167	F8	5.822	0.016	1.424E−01	1.71E−02	…	…	3.520E−02	1.02E−03	2.53E+01	3.60E+00
HD 101452	A2	6.897	0.018	…	…	…	…	1.249E−02	3.55E−04	2.17E+01	3.49E+00
HD 101472	G0	6.130	0.017	1.148E−01	1.95E−02	…	…	2.649E−02	7.91E−04	4.17E+01	1.10E+01

TABLE 5 (*Continued*)

Name	Spectral Type	Super-K_s[a] (mag)	Unc. (mag)	$f_\nu(12\ \mu m)$[b] (Jy)	Unc. (Jy)	$f_\nu(25\ \mu m)$[b] (Jy)	Unc. (Jy)	Predictions			
								$f_\nu(24\ \mu m)$[c] (Jy)	Unc. (Jy)	$bkgd_{24}$[d] (MJy sr^{-1})	Unc. (MJy sr^{-1})
HD 101959	G0 V	5.617	0.015	1.486E−01	1.93E−02	…	…	4.218E−02	1.20E−03	2.55E+01	4.66E+00
HD 102647	A3 V	1.894	0.028	4.852E+00	2.91E−01	…	…	1.268E+00	3.90E−02	4.30E+01	9.18E+00
HD 102870	F9 V	2.226	0.179	3.622E+00	2.54E−01	…	…	9.641E−01	6.34E−02	5.00E+01	1.38E+01
HD 105707	K2 III	0.071	0.028	3.017E+01	1.81E+00	7.014E+00	4.21E−01	7.568E+00	2.09E−01	3.15E+01	6.42E+00
HD 105805	A4 V	5.607	0.022	…	…	…	…	4.099E−02	1.28E−03	3.05E+01	4.32E+00
HD 106252	G0 V	5.947	0.018	1.240E−01	1.86E−02	…	…	3.130E−02	9.47E−04	4.43E+01	9.84E+00
HD 106965	A2	7.300	0.017	…	…	…	…	8.620E−03	2.40E−04	4.96E+01	1.31E+01
HD 108799	G1.5 V	4.864	0.016	3.295E−01	2.97E−02	…	…	8.498E−02	2.40E−03	4.19E+01	1.05E+01
HD 108903	M3.5 III	−3.196	0.098	…	…	…	…	1.498E+02	1.51E+01	2.05E+01	3.56E+00
HD 108944	F8	5.997	0.012	1.408E−01	2.11E−02	…	…	3.000E−02	8.21E−04	2.68E+01	3.13E+00
HD 109612	K1/K2 III	5.067	0.014	…	…	…		7.419E−02	1.95E−03	2.50E+01	3.53E+00
HD 109866	K0 III	5.264	0.016	…	…	…	…	6.188E−02	1.70E−03	2.79E+01	3.55E+00
HD 110304	A1 IV	2.052	0.028	3.962E+00	1.98E−01	9.505E−01	4.75E−02	1.075E+00	2.73E−02	2.12E+01	3.93E+00
HD 112196	F8 V	5.553	0.017	1.769E−01	1.95E−02	…	…	4.505E−02	1.32E−03	3.02E+01	3.86E+00
HD 115043	G1 V	5.334	0.014	1.706E−01	1.71E−02	…	…	5.392E−02	1.49E−03	1.81E+01	1.51E+00
HD 115780	G8/K0 III	6.237	0.016	…	…	…	…	2.525E−02	6.93E−04	3.54E+01	3.83E+00
HD 116706	A3 IV	5.489	0.015	1.670E−01	2.50E−02	…	…	4.569E−02	1.20E−03	2.69E+01	2.89E+00
HD 119545	K1 III	6.077	0.013	…	…	…	…	2.926E−02	7.55E−04	6.54E+01	4.01E+00
HD 120477	K5.5 III	0.317	0.028	2.360E+01	1.42E+00	5.362E+00	3.22E−01	5.961E+00	1.64E−01	3.03E+01	4.43E+00
HD 120933	K5 III	0.150	0.028	3.300E+01	1.98E+00	7.983E+00	5.59E−01	7.377E+00	2.10E−01	2.15E+01	1.40E+00
HD 121370	G0 IV	1.272	0.028	9.781E+00	1.56E+00	…	…	2.328E+00	8.52E−02	2.83E+01	3.81E+00
HD 121504	G2 V	6.167	0.047	…	…	…	…	2.551E−02	1.36E−03	2.22E+01	4.45E+00
HD 122652	F8	5.855	0.015	1.293E−01	1.94E−02	…	…	3.402E−02	9.76E−04	2.20E+01	1.74E+00
HD 123123	K2 III	0.634	0.028	1.644E+01	8.22E−01	3.837E+00	2.30E−01	4.352E+00	1.15E−01	3.90E+01	9.60E+00
HD 123139	K0 IIIb	−0.285	0.149	4.074E+01	2.04E+00	9.471E+00	5.68E−01	1.062E+01	4.03E−01	3.09E+01	7.05E+00
HD 124897	K1.5 III	−2.951	0.116	5.324E+02	4.79E+01	1.117E+02	7.82E+00	1.273E+02	6.46E+00	2.68E+01	3.57E+00
HD 127665	K3 III	0.582	0.028	1.773E+01	1.06E+00	4.187E+00	2.51E−01	4.631E+00	1.28E−01	2.15E+01	1.96E+00
HD 128620	G2 V	−1.922	0.146	…	…	…	…	4.389E+01	6.50E+00	3.59E+01	4.50E+00
HD 128998	A1 V	5.757	0.013	1.139E−01	1.14E−02	…	…	3.534E−02	8.76E−04	1.70E+01	7.99E−01
HD 129078	K2.5 III	0.679	0.210	1.737E+01	5.21E−01	4.261E+00	1.28E−01	4.636E+00	1.05E−01	1.78E+01	3.49E+00
HD 129655	A2	6.702	0.018	…	…	…	…	1.495E−02	4.25E−04	4.17E+01	9.95E+00
HD 131873	K4 III	−1.359	0.141	1.137E+02	4.55E+00	2.693E+01	1.08E+00	2.974E+01	8.58E−01	1.56E+01	2.10E+00
HD 131986	K0/K1 III	6.852	0.016	…	…	…	…	1.433E−02	3.93E−04	4.98E+01	4.79E+00
HD 132417	K0/K1 III	6.388	0.013	…	…	…	…	2.197E−02	5.67E−04	4.74E+01	4.82E+00
HD 132439	K2 III	5.679	0.014	…	…	…	…	4.222E−02	1.11E−03	3.32E+01	4.88E+00
HD 134493	K0 III	3.922	0.120	8.047E−01	3.22E−02	1.775E−01	1.24E−02	2.083E−01	7.10E−03	1.68E+01	9.05E−01
HD 136422	K5 III	−0.171	0.231	3.514E+01	1.41E+00	8.305E+00	4.15E−01	9.214E+00	2.93E−01	3.61E+01	9.21E+00
HD 137759	K2 III	0.584	0.028	1.634E+01	6.54E−01	4.026E+00	1.61E−01	4.464E+00	1.02E−01	1.61E+01	1.25E+00
HD 138265	K5 III	1.523	0.177	3.644E+00	1.09E−01	9.313E−01	3.72E−02	9.848E−01	2.46E−02	1.60E+01	1.39E+00
HD 139063	K5 III	0.227	0.230	2.145E+01	1.07E+00	5.265E+00	3.16E−01	5.723E+00	2.21E−01	4.52E+01	1.24E+01
HD 139698	G8/K0 III	7.136	0.019	…	…	…	…	1.103E−02	3.23E−04	4.62E+01	5.78E+00
HD 140573	K2 IIIb	−0.036	0.028	2.850E+01	1.14E+00	7.028E+00	4.22E−01	7.836E+00	1.94E−01	2.99E+01	6.06E+00
HD 141477	M0.5 III	−0.016	0.028	3.110E+01	1.55E+00	7.606E+00	3.80E−01	8.139E+00	2.07E−01	2.36E+01	3.83E+00
HD 141937	G2.5 V	5.772	0.013	1.221E−01	1.71E−02	…	…	3.649E−02	1.01E−03	5.05E+01	1.40E+01
HD 144873	G5	6.913	0.013	…	…	…	…	1.283E−02	3.63E−04	1.86E+01	2.16E+00
HD 145829	K2 III	5.142	0.018	…	…	…	…	6.923E−02	1.98E−03	6.27E+01	6.67E+00
HD 146051	M0.5 III	−1.281	0.028	1.077E+02	5.38E+00	2.600E+01	1.30E+00	2.693E+01	6.87E−01	3.69E+01	8.99E+00
HD 149447	K6 III	0.356	0.226	…	…	…	…	5.685E+00	1.29E+00	4.21E+01	1.13E+01
HD 150039	K0 III	4.872	0.013	…	…	…	…	8.878E−02	2.29E−03	6.09E+01	8.06E+00
HD 150680	G0 IV	1.174	0.183	9.061E+00	4.53E−01	2.246E+00	1.35E−01	2.447E+00	9.38E−02	1.87E+01	2.68E+00
HD 150706	G0	5.559	0.018	1.571E−01	9.42E−03	…	…	4.401E−02	1.21E−03	1.58E+01	2.30E+00
HD 150798	K2 II–III	−1.140	0.133	1.036E+02	3.11E+00	2.355E+01	7.06E−01	2.655E+01	5.95E−01	2.04E+01	4.43E+00
HD 151249	K5 III	−0.039	0.242	…	…	…	…	8.179E+00	1.99E+00	2.40E+01	5.54E+00
HD 151680	K2.5 III	−0.389	0.140	…	…	…	…	1.129E+01	1.60E+00	4.35E+01	1.19E+01
HD 152222	K2 III	3.748	0.150	1.365E+00	8.19E−02	3.077E−01	1.85E−02	3.362E−01	1.40E−02	1.53E+01	2.00E+00
HD 153210	K2 III	0.549	0.028	1.735E+01	8.68E−01	4.033E+00	2.02E−01	4.635E+00	1.18E−01	2.60E+01	5.51E+00
HD 153458	G0	6.456	0.013	…	…	…	…	1.955E−02	5.52E−04	3.98E+01	1.02E+01
HD 154391	K2 III	4.032	0.111	7.627E−01	2.29E−02	1.923E−01	9.61E−03	2.030E−01	5.28E−03	1.50E+01	2.02E+00
HD 156283	K3 Iab	−0.012	0.028	3.320E+01	1.33E+00	7.700E+00	3.85E−01	8.321E+00	1.99E−01	1.74E+01	2.71E+00
HD 158460	A2 V	5.489	0.013	1.610E−01	8.05E−03	…	…	4.529E−02	1.03E−03	1.53E+01	2.04E+00
HD 158485	A4 V	6.136	0.016	7.908E−02	8.70E−03	…	…	2.489E−02	6.59E−04	1.50E+01	1.76E+00

TABLE 5 (*Continued*)

Name	Spectral Type	Super-K_s[a] (mag)	Unc. (mag)	f_ν(12 μm)[b] (Jy)	Unc. (Jy)	f_ν(25 μm)[b] (Jy)	Unc. (Jy)	Predictions			
								f_ν(24 μm)[c] (Jy)	Unc. (Jy)	bkgd$_{24}$[d] (MJy sr^{-1})	Unc. (MJy sr^{-1})
HD 159048	K0 III	4.122	0.236	8.951E−01	2.68E−02	2.302E−01	1.15E−02	2.391E−01	6.36E−03	1.56E+01	1.98E+00
HD 159222	G5 V	4.977	0.013	2.604E−01	1.56E−02	…	…	7.483E−02	1.92E−03	1.77E+01	2.99E+00
HD 159330	K2 III	2.867	0.146	2.065E+00	6.19E−02	4.976E−01	1.99E−02	5.467E−01	1.35E−02	1.49E+01	1.71E+00
HD 161096	K2 III	0.129	0.028	2.645E+01	1.32E+00	6.129E+00	3.06E−01	6.943E+00	1.77E−01	2.81E+01	6.63E+00
HD 161743	B9 IV	7.585	0.018	…	…	…	…	6.630E−03	1.89E−04	4.07E+01	1.10E+01
HD 163376	M0 III	0.748	0.229	…	…	…	…	3.962E+00	9.12E−01	3.65E+01	9.80E+00
HD 163466	A2 V	6.364	0.013	8.919E−02	1.07E−02	…	…	2.053E−02	5.14E−04	1.53E+01	2.16E+00
HD 163588	K2 III	0.971	0.028	1.165E+01	3.49E−01	2.853E+00	8.56E−02	3.142E+00	6.02E−02	1.49E+01	1.82E+00
HD 164058	K5 III	−1.408	0.028	1.106E+02	3.32E+00	2.713E+01	8.14E−01	2.931E+01	5.62E−01	1.56E+01	2.38E+00
HD 165459	A2?	6.604	0.027	7.533E−02	1.20E−02	…	…	1.649E−02	5.62E−04	1.54E+01	2.21E+00
HD 166780	K4.5 III	3.792	0.101	7.866E−01	3.15E−02	1.919E−01	1.34E−02	2.104E−01	7.07E−03	1.49E+01	1.88E+00
HD 167389	F8	5.908	0.015	1.118E−01	1.01E−02	…	…	3.210E−02	8.93E−04	1.66E+01	2.94E+00
HD 169916	K1 IIIb	0.298	0.028	…	…	…	…	5.997E+00	2.15E−01	5.08E+01	1.36E+01
HD 170693	K1.5 III	2.147	0.159	5.002E+00	1.50E−01	1.187E+00	3.56E−02	1.311E+00	2.95E−02	1.53E+01	2.31E+00
HD 172066	G5?	6.279	0.015	8.687E−02	8.69E−03	…	…	2.302E−02	6.46E−04	1.54E+01	2.35E+00
HD 172728	A0 V	5.748	0.013	1.326E−01	1.06E−02	…	…	3.602E−02	8.78E−04	1.53E+01	2.36E+00
HD 173398	K0 III	4.003	0.213	8.061E−01	3.22E−02	1.912E−01	1.15E−02	2.120E−01	7.13E−03	1.54E+01	2.38E+00
HD 173511	K5 III	3.892	0.134	8.253E−01	2.48E−02	1.945E−01	9.73E−03	2.163E−01	5.67E−03	1.54E+01	2.39E+00
HD 173976	K5 III	3.572	0.177	1.186E+00	3.56E−02	2.966E−01	1.19E−02	3.163E−01	7.87E−03	1.53E+01	2.43E+00
HD 174123	G5?	6.587	0.014	5.984E−02	8.98E−03	…	…	1.727E−02	4.87E−04	1.54E+01	2.39E+00
HD 175510	A0 V	4.960	0.124	2.920E−01	2.04E−02	…	…	7.833E−02	4.82E−03	2.76E+01	6.66E+00
HD 176841	G5?	6.121	0.016	9.380E−02	1.22E−02	…	…	2.652E−02	7.69E−04	1.54E+01	2.44E+00
HD 177716	K1 IIIb	0.495	0.213	1.861E+01	9.30E−01	4.201E+00	2.10E−01	4.785E+00	1.71E−01	4.97E+01	1.38E+01
HD 180093	K0 Iab	5.081	0.015	5.662E+01	2.83E+00	1.862E+01	9.31E−01	7.340E−02	1.97E−03	4.44E+01	1.25E+01
HD 180711	G9 III	0.734	0.028	1.495E+01	4.49E−01	3.583E+00	1.08E−01	3.974E+00	7.62E−02	1.52E+01	2.74E+00
HD 181655	G8 V	4.625	0.013	3.838E−01	2.30E−02	9.729E−02	1.46E−02	1.097E−01	2.57E−03	1.73E+01	3.43E+00
HD 183439	M0 III	0.478	0.028	…	…	…	…	5.081E+00	1.82E−01	2.15E+01	4.37E+00
HD 186791	K3 II	−0.572	0.028	…	…	…	…	1.336E+01	4.78E−01	2.60E+01	6.18E+00
HD 189276	K5 Iab	0.785	0.168	9.434E+00	3.77E−01	2.417E+00	9.67E−02	2.581E+00	7.50E−02	1.54E+01	2.64E+00
HD 191854	G5	5.808	0.015	…	…	…	…	3.551E−02	1.04E−03	1.92E+01	3.13E+00
HD 193017	F8	5.949	0.013	1.381E−01	1.93E−02	…	…	3.134E−02	8.69E−04	3.73E+01	1.05E+01
HD 195034	G5	5.547	0.017	…	…	…	…	4.516E−02	1.37E−03	2.14E+01	4.83E+00
HD 197989	K0 III	0.047	0.028	…	…	…	…	7.556E+00	2.70E−01	1.89E+01	3.86E+00
HD 198542	M0 III	0.209	0.198	2.784E+01	1.39E+00	6.685E+00	3.34E−01	7.318E+00	2.61E−01	4.70E+01	1.30E+01
HD 199598	G0 V	5.449	0.015	1.923E−01	1.54E−02	…	…	4.961E−02	1.36E−03	2.08E+01	4.47E+00
HD 200914	K5/M0 III	0.513	0.185	2.049E+01	1.23E+00	5.094E+00	3.06E−01	5.466E+00	2.30E−01	4.78E+01	1.32E+01
HD 201941	A2	6.634	0.016	…	…	…	…	1.592E−02	4.33E−04	3.36E+01	8.94E+00
HD 204277	F8 V	5.416	0.015	2.114E−01	2.32E−02	…	…	5.124E−02	1.45E−03	2.54E+01	5.90E+00
HD 205772	A5 IV	7.651	0.013	…	…	…	…	6.239E−03	1.60E−04	3.13E+01	7.06E+00
HD 205905	G4 V	5.325	0.018	2.481E−01	2.98E−02	…	…	5.587E−02	1.67E−03	4.36E+01	1.15E+01
HD 209750	G2 Ib	0.917	0.028	1.383E+01	8.30E−01	3.014E+00	1.81E−01	3.430E+00	9.46E−02	4.08E+01	1.12E+01
HD 209952	B7 IV	2.003	0.213	3.743E+00	1.50E−01	8.486E−01	5.09E−02	1.014E+00	3.42E−02	2.64E+01	5.30E+00
HD 211416	K3 III	−0.330	0.183	4.280E+01	1.71E+00	1.024E+01	4.10E−01	1.128E+01	3.28E−01	2.12E+01	3.80E+00
HD 212291	G5	6.263	0.020	…	…	…	…	2.335E−02	7.49E−04	3.29E+01	8.06E+00
HD 213310	M0 II+	0.158	0.028	…	…	…	…	6.822E+00	2.44E−01	1.76E+01	2.76E+00
HD 216032	K5 III	0.167	0.028	2.674E+01	1.60E+00	6.646E+00	3.99E−01	6.923E+00	1.91E−01	4.98E+01	1.35E+01
HD 216131	G8 II	1.374	0.028	8.362E+00	5.02E−01	1.989E+00	1.19E−01	2.217E+00	6.11E−02	2.51E+01	4.94E+00
HD 216275	G0	5.782	0.013	…	…	…	…	3.637E−02	1.03E−03	1.77E+01	2.94E+00
HD 217014	G2.5 I	3.873	0.028	7.502E−01	4.50E−02	1.715E−01	2.23E−02	2.137E−01	6.42E−03	2.74E+01	5.67E+00
HD 217382	K4 III	1.471	0.193	8.334E+00	2.50E−01	1.936E+00	1.36E−01	2.176E+00	6.15E−02	1.75E+01	2.66E+00
HD 217906	M2.5 II	−2.190	0.028	2.702E+02	1.35E+01	6.888E+01	3.44E+00	6.472E+01	1.66E+00	2.41E+01	4.45E+00
HD 60178J	A2 V	1.431	0.028	7.211E+00	4.33E−01	1.624E+00	8.12E−02	1.893E+00	5.01E−02	4.50E+01	1.22E+01
HD 98230J	G0 V	2.090	0.187	4.069E+00	2.03E−01	8.779E−01	5.27E−02	1.036E+00	3.98E−02	3.15E+01	5.37E+00
NPM1 +61.0569	K0.5 III	7.210	0.013	…	…	…	…	1.031E−02	2.66E−04	1.53E+01	2.04E+00
NPM1 +68.0412	K2 III	7.169	0.015	…	…	…	…	1.070E−02	2.87E−04	1.54E+01	2.34E+00
SAO 9310	K0	7.332	0.014	…	…	…	…	9.211E−03	2.42E−04	1.58E+01	2.41E+00

[a] Super-K_s is the weighted average of J (transformed to K_s) and K_s (see § 4.1).

[b] Taken from the *IRAS* Faint Source Catalog and modified as discussed in § 4.1.3.

[c] These flux densities apply to the effective wavelength of the 24 μm band, 23.675 μm.

[d] See § 4.3.

TABLE 6
COMBINED MEASUREMENTS AND CALIBRATION FACTORS

Name	Number of Measurements	24 μm Count Rate[a] (DN s^{-1})	Uncertainty (DN s^{-1})	Calibration Factor (MJy sr^{-1} [DN s^{-1}]$^{-1}$)	Uncertainty (MJy sr^{-1} [DN s^{-1}]$^{-1}$)
BD +621644	1	1.033E+04	5.19E+01	4.037E−02	9.72E−04
HD 000319	1	6.708E+03	5.00E+01	4.262E−02	1.16E−03
HD 001160	1	1.395E+03	1.56E+01	5.250E−02	1.60E−03
HD 001644	1	8.191E+03	5.69E+01	4.534E−02	1.25E−03
HD 002151	1	3.271E+05	1.23E+03	4.573E−02	1.46E−03
HD 002811	1	1.591E+03	3.35E+01	4.331E−02	1.51E−03
HD 008941	1	7.202E+03	3.46E+01	4.948E−02	1.40E−03
HD 009927	1	6.045E+05	2.45E+03	4.539E−02	1.17E−03
HD 011413	1	7.866E+03	3.87E+01	3.856E−02	9.81E−04
HD 014943	1	7.180E+03	2.84E+01	4.192E−02	1.14E−03
HD 015008	5	2.719E+04	1.21E+01	4.757E−02	1.67E−03
HD 015646	1	2.997E+03	4.84E+01	4.349E−02	1.36E−03
HD 017254	5	4.622E+03	1.02E+01	4.368E−02	1.10E−03
HD 019019	1	6.204E+03	3.74E+01	4.714E−02	1.41E−03
HD 020722	1	5.818E+03	4.56E+01	3.517E−02	9.62E−04
HD 020888	2	5.519E+03	2.04E+01	4.407E−02	1.19E−03
HD 020902	1	6.872E+05	2.62E+03	4.361E−02	1.56E−03
HD 021981	1	6.089E+03	1.33E+01	4.447E−02	1.22E−03
HD 025860	1	4.202E+03	3.26E+01	4.031E−02	1.08E−03
HD 027466	1	3.146E+03	3.18E+01	4.846E−02	1.46E−03
HD 028099	1	2.546E+03	2.80E+01	4.635E−02	1.47E−03
HD 028471	1	3.173E+03	1.81E+01	4.590E−02	1.39E−03
HD 029461	1	2.759E+03	2.77E+01	4.736E−02	1.62E−03
HD 030246	1	2.497E+03	2.75E+01	4.011E−02	1.38E−03
HD 032831	1	2.301E+05	8.06E+02	4.509E−02	8.79E−04
HD 034868	1	3.851E+03	3.89E+01	4.791E−02	1.46E−03
HD 035666	1	3.416E+04	1.34E+02	4.578E−02	1.52E−03
HD 036167	1	5.627E+05	2.23E+03	4.301E−02	2.54E−03
HD 037962	1	3.281E+03	3.12E+01	4.565E−02	1.39E−03
HD 038949	1	2.871E+03	3.10E+01	4.602E−02	1.51E−03
HD 039608	6	3.861E+04	1.25E+01	4.455E−02	1.46E−03
HD 040129	1	2.025E+03	2.04E+01	4.609E−02	1.43E−03
HD 040335	1	2.866E+03	3.25E+01	4.383E−02	1.27E−03
HD 041371	4	1.498E+04	1.16E+01	4.373E−02	1.00E−03
HD 042525	1	5.116E+03	2.85E+01	4.460E−02	1.14E−03
HD 042701	2	4.346E+04	1.20E+02	4.515E−02	8.27E−04
HD 043107	14	8.368E+03	1.16E+01	4.660E−02	1.07E−03
HD 044594	1	9.411E+03	4.79E+01	4.631E−02	1.30E−03
HD 045557	1	5.492E+03	3.51E+01	4.228E−02	1.06E−03
HD 046190	1	3.703E+03	2.82E+01	3.518E−02	9.61E−04
HD 046819	1	8.504E+03	4.94E+01	4.627E−02	1.15E−03
HD 047332	1	2.595E+03	2.60E+01	3.852E−02	1.05E−03
HD 050310	1	7.865E+05	2.88E+03	5.228E−02	1.54E−03
HD 053501	4	1.838E+05	3.71E+02	4.531E−02	1.03E−03
HD 057336	1	1.403E+03	3.44E+01	4.446E−02	1.71E−03
HD 058142	1	1.458E+04	1.33E+02	4.686E−02	2.57E−03
HD 060178	1	2.584E+05	7.17E+02	4.808E−02	1.28E−03
HD 061929	1	3.038E+03	2.66E+01	4.569E−02	1.35E−03
HD 064324	1	3.672E+03	3.87E+01	4.256E−02	1.28E−03
HD 065517	1	2.122E+03	1.81E+01	3.928E−02	1.19E−03
HD 066751	1	9.671E+03	2.80E+01	4.704E−02	1.30E−03
HD 069863	1	1.240E+04	5.52E+01	4.140E−02	9.15E−04
HD 073210	1	3.707E+03	5.55E+01	4.261E−02	1.30E−03
HD 073666	1	2.541E+03	5.66E+01	4.584E−02	1.59E−03
HD 073819	1	3.170E+03	5.29E+01	4.553E−02	1.41E−03
HD 077281	1	1.673E+03	1.99E+01	4.374E−02	1.30E−03
HD 080007	2	2.594E+05	6.64E+02	4.536E−02	1.33E−03
HD 082308	1	7.022E+05	2.59E+03	4.484E−02	1.32E−03
HD 082621	1	1.909E+04	8.24E+01	4.679E−02	2.47E−03
HD 087901	1	2.350E+05	7.87E+02	4.929E−02	1.39E−03
HD 091375	1	1.602E+04	6.73E+01	4.646E−02	2.18E−03

TABLE 6 (*Continued*)

Name	Number of Measurements	24 μm Count Rate[a] (DN s^{-1})	Uncertainty (DN s^{-1})	Calibration Factor (MJy sr^{-1} [DN s^{-1}]$^{-1}$)	Uncertainty (MJy sr^{-1} [DN s^{-1}]$^{-1}$)
HD 092788	1	5.299E+03	3.93E+01	4.713E−02	1.64E−03
HD 092845	1	7.166E+03	4.51E+01	3.975E−02	1.08E−03
HD 096833	2	7.426E+05	2.07E+03	4.910E−02	1.26E−03
HD 098230	1	1.467E+05	4.65E+02	4.635E−02	1.78E−03
HD 098553	1	3.858E+03	3.39E+01	4.732E−02	1.41E−03
HD 100167	1	5.036E+03	3.57E+01	4.587E−02	1.36E−03
HD 101452	1	1.910E+03	3.50E+01	4.292E−02	1.45E−03
HD 101472	1	3.834E+03	3.44E+01	4.534E−02	1.41E−03
HD 101959	1	5.822E+03	3.20E+01	4.755E−02	1.38E−03
HD 102647	2	2.365E+05	5.09E+02	3.519E−02	1.08E−03
HD 102870	1	1.309E+05	5.02E+02	4.834E−02	3.18E−03
HD 105805	1	5.734E+03	5.10E+01	4.692E−02	1.52E−03
HD 106252	1	4.749E+03	3.73E+01	4.326E−02	1.35E−03
HD 106965	1	1.248E+03	1.87E+01	4.533E−02	1.43E−03
HD 108799	1	1.242E+04	4.16E+01	4.490E−02	1.28E−03
HD 108944	1	4.431E+03	3.10E+01	4.443E−02	1.25E−03
HD 109612	1	1.260E+04	6.56E+01	3.864E−02	1.04E−03
HD 109866	1	4.368E+03	2.77E+01	9.297E−02	2.62E−03
HD 110304	1	1.510E+05	5.70E+02	4.672E−02	1.20E−03
HD 112196	1	6.345E+03	3.41E+01	4.660E−02	1.39E−03
HD 115043	1	7.863E+03	3.29E+01	4.500E−02	1.26E−03
HD 115780	2	1.041E+04	9.28E+01	1.592E−02	4.59E−04
HD 116706	1	6.188E+03	5.01E+01	4.846E−02	1.33E−03
HD 119545	1	1.360E+05	2.33E+03	1.412E−03	4.37E−05
HD 121370	1	3.132E+05	1.17E+03	4.878E−02	1.80E−03
HD 121504	1	4.016E+03	4.34E+01	4.169E−02	2.27E−03
HD 122652	1	5.100E+03	2.87E+01	4.378E−02	1.28E−03
HD 123123	1	6.343E+05	2.39E+03	4.503E−02	1.20E−03
HD 127665	1	6.687E+05	2.51E+03	4.545E−02	1.26E−03
HD 128998	1	4.824E+03	2.79E+01	4.808E−02	1.22E−03
HD 129655	1	2.577E+03	2.87E+01	3.807E−02	1.16E−03
HD 131986	1	7.721E+03	9.91E+01	1.218E−02	3.69E−04
HD 132417	1	5.041E+03	5.49E+01	2.860E−02	8.01E−04
HD 132439	1	5.055E+03	3.77E+01	5.481E−02	1.50E−03
HD 134493	1	2.956E+04	1.24E+02	4.625E−02	1.59E−03
HD 138265	2	1.446E+05	4.23E+02	4.470E−02	1.12E−03
HD 139698	1	8.006E+03	1.99E+02	9.042E−03	3.47E−04
HD 141937	1	5.126E+03	3.82E+01	4.672E−02	1.34E−03
HD 144873	1	1.723E+03	1.96E+01	4.887E−02	1.49E−03
HD 150680	1	3.335E+05	1.33E+03	4.815E−02	1.86E−03
HD 150706	1	6.656E+03	3.12E+01	4.339E−02	1.21E−03
HD 152222	3	5.150E+04	1.92E+01	4.284E−02	1.79E−03
HD 153458	1	2.799E+03	3.91E+01	4.584E−02	1.44E−03
HD 154391	1	3.023E+04	1.22E+02	4.407E−02	1.16E−03
HD 158460	1	7.931E+03	5.71E+01	3.748E−02	8.97E−04
HD 158485	1	3.564E+03	2.80E+01	4.583E−02	1.27E−03
HD 159048	1	3.600E+04	1.88E+02	4.359E−02	1.18E−03
HD 159222	5	1.010E+04	1.02E+01	4.862E−02	1.25E−03
HD 159330	102	7.929E+04	1.65E+01	4.525E−02	1.12E−03
HD 163466	3	2.938E+03	1.90E+01	4.586E−02	1.19E−03
HD 163588	2	4.479E+05	1.34E+03	4.604E−02	8.93E−04
HD 165459	2	3.843E+03	2.48E+01	2.816E−02	9.77E−04
HD 166780	2	3.065E+04	8.84E+01	4.505E−02	1.52E−03
HD 167389	1	4.449E+03	2.66E+01	4.735E−02	1.35E−03
HD 170693	4	1.855E+05	2.14E+01	4.638E−02	1.04E−03
HD 172066	1	3.368E+03	2.68E+01	4.486E−02	1.31E−03
HD 172728	2	4.747E+03	2.21E+01	4.980E−02	1.24E−03
HD 173398	46	3.031E+04	1.84E+01	4.590E−02	1.54E−03
HD 173511	1	3.165E+04	1.24E+02	4.485E−02	1.19E−03
HD 173976	1	4.749E+04	1.72E+02	4.371E−02	1.10E−03
HD 174123	1	2.296E+03	2.39E+01	4.936E−02	1.48E−03

TABLE 6 (*Continued*)

Name	Number of Measurements	24 μm Count Rate[a] (DN s^{-1})	Uncertainty (DN s^{-1})	Calibration Factor (MJy sr^{-1} [DN s^{-1}]$^{-1}$)	Uncertainty (MJy sr^{-1} [DN s^{-1}]$^{-1}$)
HD 176841	1	3.644E+03	2.79E+01	4.776E−02	1.43E−03
HD 180711	2	5.759E+05	1.47E+03	4.529E−02	8.76E−04
HD 183439	2	7.200E+05	2.64E+03	4.631E−02	1.67E−03
HD 189276	2	3.857E+05	1.02E+03	4.392E−02	1.28E−03
HD 191854	3	4.867E+03	1.97E+01	4.788E−02	1.41E−03
HD 193017	1	4.150E+03	3.86E+01	4.956E−02	1.45E−03
HD 195034	1	6.127E+03	3.33E+01	4.837E−02	1.49E−03
HD 199598	1	7.021E+03	3.60E+01	4.637E−02	1.30E−03
HD 201941	1	2.900E+03	2.79E+01	3.603E−02	1.04E−03
HD 204277	1	7.301E+03	2.83E+01	4.606E−02	1.31E−03
HD 205905	1	7.871E+03	3.42E+01	4.658E−02	1.41E−03
HD 209952	2	1.465E+05	3.74E+02	4.542E−02	1.54E−03
HD 212291	1	3.319E+03	3.19E+01	4.617E−02	1.55E−03
HD 216131	1	3.277E+05	1.24E+03	4.440E−02	1.24E−03
HD 216275	1	5.062E+03	4.07E+01	4.715E−02	1.39E−03
HD 217382	1	3.264E+05	1.18E+03	4.375E−02	1.25E−03
NPM1 +61.0569	1	1.510E+03	1.64E+01	4.481E−02	1.25E−03
NPM1 +68.0412	1	1.494E+03	1.67E+01	4.700E−02	1.37E−03
SAO 9310	1	1.069E+03	1.24E+01	5.655E−02	1.63E−03

[a] The count rates in this table can be converted to janskys by multiplying by the product of the aperture correction, calibration factor, and pixel area discussed in the text, or a factor of 6.92×10^{-6}.

TABLE 7
STARS REJECTED AS 24 μm CALIBRATORS

Name	Reason for Rejection
BD +621644	Calibration factor 12% low
HD 011413	Calibration factor 18% low[a]
HD 020722	Double source[b]
HD 046190	Calibration factor 29% low[c]
HD 047332	Calibration factor 18% low[a]
HD 065517	Calibration factor 16% low[a]
HD 092845	Double star
HD 102647	Calibration factor 29% low[c]
HD 109612	Bright, complex background
HD 109866	Bright, complex background
HD 115780	Bright, complex background
HD 119545	Bright, complex background
HD 129655	Calibration factor 19% low[a]
HD 131986	Bright, complex background and nearby contaminating sources
HD 132417	Bright, complex background and nearby contaminating sources
HD 132439	Bright, complex background
HD 139698	Bright, complex background
HD 158460	Calibration factor 21% low[c]
HD 165459	Calibration factor 61% low[c]
HD 201941	Calibration factor 26% low[d]
SAO 9310	Calibration factor 20% high

[a] NIR measurements indicate that this star is reddened, so the predicted flux is likely low.

[b] There is a 24 μm source 14″ to the north of this star. SIMBAD does not indicate that the star is part of a multiple system and the *Spitzer* Planning and Observation Tool (SPOT) does not indicate any asteroids in the field, so the source is likely a background galaxy.

[c] Su et al. (2006) find that this source has a debris disk.

[d] This star is not known to be part of a multiple system and no asteroids were expected in the field, so this star likely has an infrared excess.

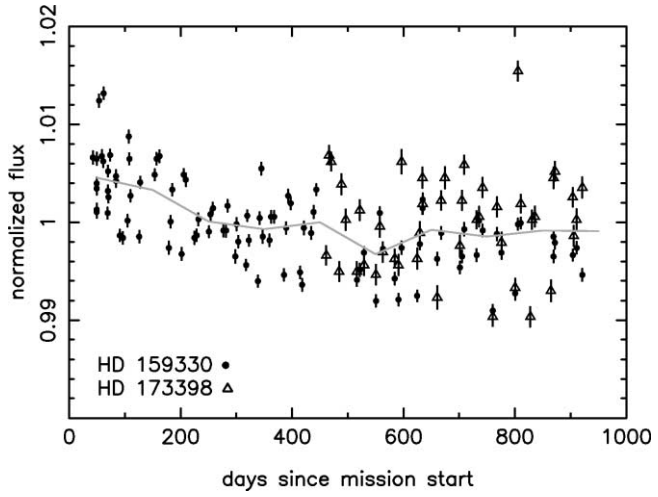

FIG. 7.—Repeatability of 24 μm photometry on two routinely monitored sources: HD 159330 (*filled circles*) and HD 173398 (*open triangles*). The gray curve is a sigma-clipped average in 10 equally spaced bins.

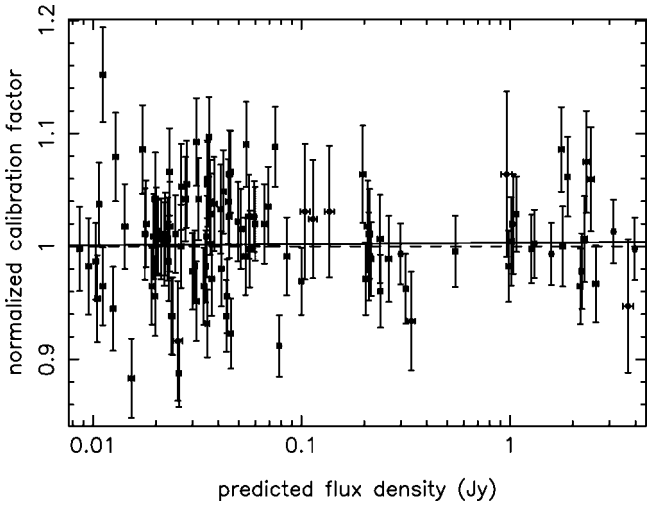

FIG. 8.—The 24 μm calibration factor normalized to the nominal calibration factor (see § 3) as a function of predicted 24 μm flux density. The error bars are drawn from Tables 5 and 6. The dashed line is drawn at 1 as a guide, while the solid line is a linear least-squares fit to the data (see § 5). Points greater than 5 σ above or below the nominal calibration factor have not been included in the plot or the fit.

(~2%–3%) amount from other infrared calibrations commonly in use. For the convenience of the reader, we present a direct comparison of our measurements to predictions in one of those systems, that prepared by Cohen and collaborators. Specifically, we compute predicted flux densities at 24 μm for the 10 "template" stars (Cohen et al. 1999 and references therein) observed by us by interpolating the values given by the templates. We adopt the model uncertainties provided by the templates. We take the "observed" values and uncertainties from Table 6 and convert them to flux densities using the calibration factor computed in § 3. We present the data used for and the results of this comparison in Table 8, where we reject the star HD 020722 due to a contaminating background source at 24 μm (cf. Table 7). The weighted average ratio of our measurements to the predictions is 1.026 ± 0.013; i.e., measurements on the Cohen et al. (1999) system can be converted to the system used by MIPS by multiplying by this factor. Much of this difference is due to the different fluxes adopted for Vega at 10.6 μm (35.03 Jy by G. H. Rieke et al. [2007, in preparation] and 34.38 Jy by Cohen et al. [1999], which differ by 2%).

5.7. Extended-Source Calibration

As demonstrated in § 2, the model PSF is a good match to the data out to large radii, so we expect the extrapolation of the calibration to infinite radii to be well understood. As a check, we compare measurements of extended sources (nearby galaxies) observed by the *Spitzer* legacy teams SINGS (*Spitzer* Infrared Nearby Galaxies Survey; Kennicutt et al. 2003) and SAGE (Surveying the Agents of a Galaxy's Evolution; Meixner et al. 2006) and by guaranteed time observers (Hinz et al. 2004; Gordon et al. 2006, 2007a) to *IRAS* measurements. We apply color corrections from Beichman et al. (1988; *IRAS*) and Stansberry et al. (2007; MIPS) assuming a power-law spectrum fit to the 12/25 or 24/70 μm data to the *IRAS* and MIPS (SINGS measurements taken from Dale et al. 2007) measurements, and also correct the MIPS measurements to the calibration factor derived in § 3. We interpolate the *IRAS* 12 and 25 μm measurements to the effective wavelength of the 24 μm band, 23.675 μm. We compare the results graphically in Figure 10. The weighted average ratio of MIPS to *IRAS* measurements

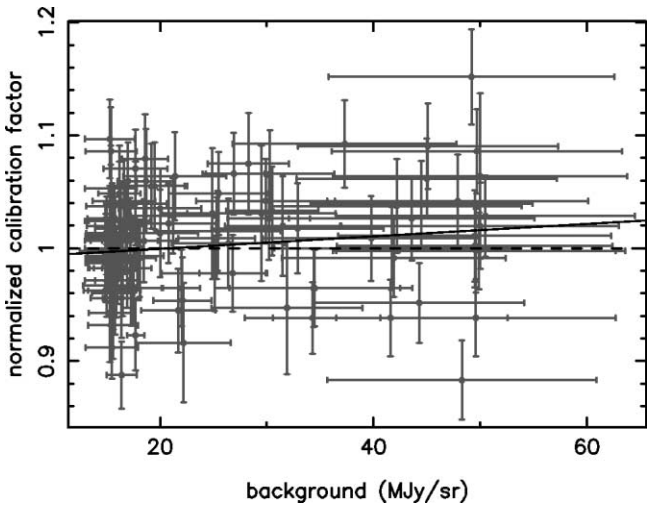

FIG. 9.—Same as Fig. 8, but as a function of predicted background.

TABLE 8
24 μm Observations of Cohen et al. Template Stars

Name	Observed		Template Prediction		Observed/ Template	Uncertainty
	f_ν(24 μm) (Jy)	Uncertainty (Jy)	f_ν(24 μm) (Jy)	Uncertainty (Jy)		
HD 032831	1.592E+00	5.58E−03	1.560E+00	5.99E−02	1.020	0.039
HD 053501	1.271E+00	2.57E−03	1.238E+00	1.08E−01	1.027	0.089
HD 163588	3.098E+00	9.27E−03	3.018E+00	1.06E−01	1.027	0.036
HD 189276	2.668E+00	7.06E−03	2.559E+00	8.31E−02	1.043	0.034
HD 138265	1.000E+00	2.93E−03	9.507E−01	3.25E−02	1.052	0.036
HD 036167	3.893E+00	1.54E−02	3.800E+00	1.27E−01	1.024	0.035
HD 170693	1.283E+00	1.48E−04	1.291E+00	4.57E−02	0.994	0.035
HD 009927	4.182E+00	1.69E−02	3.908E+00	2.94E−01	1.070	0.081
HD 134493	2.045E−01	8.58E−04	2.017E−01	6.90E−03	1.014	0.035

Note.—The star HD 020722 has a template and was observed at 24 μm but was not included in this comparison due to a nearby source at 24 μm (cf. Table 7).

is 0.96, well within the 8% combined uncertainty of both instruments.

6. SUMMARY

We discuss the flux calibration of the MIPS 24 μm band, which is based on stars. We describe the data reduction and photometric procedures that we use for the calibration sources, which produce fluxes that are 1.6% $\pm$ 0.6% lower than those achieved by the automated pipeline at the *Spitzer* Science Center. We show that the calibration of the two imaging modes, photometry and scan map, is consistent within 1%.

We compute the calibration factor (the conversion from count rate to physical units) for the MIPS 24 μm band, using a sample of 22 A stars that has been well measured and has been carefully vetted to exclude debris disk systems. We find a value of 4.54×10^{-2} MJy sr^{-1} (DN s^{-1})$^{-1}$, with an uncertainty of 2%. Based on this uncertainty and the difference between the SSC pipeline and the DAT discussed in § 2.5 and summarized above, we recommend that a net uncertainty on the calibration of 4% is appropriate for general use.

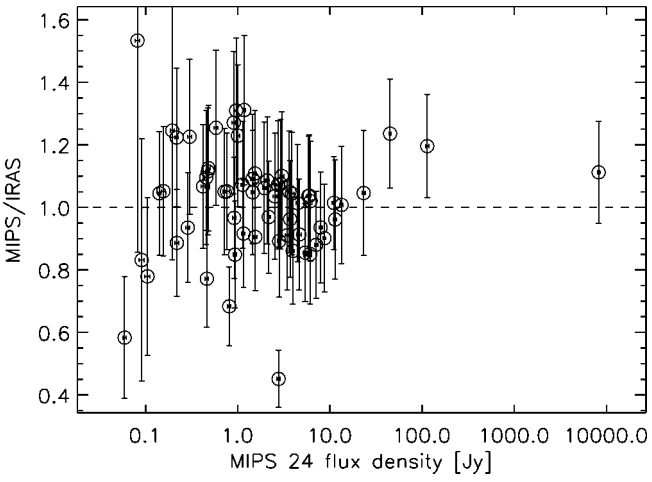

Fig. 10.—Ratio of MIPS to *IRAS* measurements of extended sources as a function of flux density measured at 24 μm. The error bars represent the combined uncertainty on both measurements. The dashed line is drawn at 1 as a guide.

We present a sample of 238 stars appropriate for use as MIPS flux calibrators. We have computed flux densities of these stars at the effective wavelength of the 24 μm band, 23.675 μm. We present 348 measurements of 141 of these stars and combine those measurements with the 24 μm predictions to test various aspects of the calibration. We find that routine monitoring of a star near the *Spitzer* constant viewing zone demonstrates that 24 μm photometry with MIPS is repeatable to 0.4%. The calibration is linear to 0.3% over a range of ~460 in flux density, and there are no significant systematic effects on the calibration due to spectral type, background, or angular extent of the source.

We thank John Carpenter for helpful discussions, especially regarding the effect of exposure time on the measured count rate. We would also like to thank the anonymous referee, whose comments improved this paper. This work is based on observations made with the *Spitzer Space Telescope*, which is operated by the Jet Propulsion Laboratory, California Institute of Technology, under NASA contract 1407. This research has made use of the SIMBAD database, operated at CDS, Strasbourg, France. This publication makes use of data products from the Two Micron All Sky Survey, which is a joint project of the University of Massachusetts and the Infrared Processing and Analysis Center/California Institute of Technology, funded by the National Aeronautics and Space Administration and the National Science Foundation. Support for this work was provided by NASA through contract 1255094 issued by JPL/Caltech.

REFERENCES

Beichman, C. A., Neugebauer, G., Habing, H. J., Clegg, P. E., & Chester, T. J. 1988, *Infrared Astronomical Satellite* (*IRAS*) Catalogs and Atlases, Vol. 1, Explanatory Supplement (Washington, DC: GPO)

Blommaert, J. A. D. L., et al. 2003, The *ISO* Handbook, Vol. 2, CAM—The *ISO* Camera (ESA SP-1262; Noordwijk: ESA)

Bryden, G., et al. 2006, ApJ, 636, 1098

Carpenter, J. M. 2001, AJ, 121, 2851

Cohen, M., Walker, R. G., Carter, B., Hammersley, P., Kidger, M., & Noguchi, K. 1999, AJ, 117, 1864

Cohen, M., Walker, R. G., Jayaraman, S., Barker, E., & Price, S. D. 2001, AJ, 121, 1180

Dale, D. A., et al. 2007, ApJ, 655, 863

Decin, L., Waelkens, C., Eriksson, K., Gustafsson, B., Plez, B., Sauval, A. J., Van Assche, W., & Vandenbussche, B. 2000, A&A, 364, 137

Fadda, D., et al. 2006, AJ, 131, 2859

Fazio, G. G., et al. 2004, ApJS, 154, 10

Gordon, K. D., Engelbracht, C. W., Smith, J.-D. T., Rieke, G. H., & Misselt, K. A. 2007a, in ASP Conf. Ser., The *Spitzer* Science Center 2005 Conf., Infrared Diagnostics of Galaxy Evolution, ed. R.-R. Chary (San Francisco: ASP), in press (astro-ph/0605544)

Gordon, K. D., et al. 2005, PASP, 117, 503

———. 2006, ApJ, 638, L87

———. 2007b, PASP, 119, 1019

Gry, C., et al. 2003, The *ISO* Handbook, Vol. 3, LWS—The Long Wavelength Spectrometer (ESA SP-1262; Noordwijk: ESA)

Hauser, M. G., Kelsall, T., Leisawitz, D., & Weiland, J. 1998, *COBE* Diffuse Infrared Background Experiment (DIRBE) Explanatory Supplement (Greenbelt: NASA)

Hinz, J. L., et al. 2004, ApJS, 154, 259

Houck, J. R., et al. 2004, ApJS, 154, 18

Johnson, H. L., Iriarte, B., Mitchell, R. I., & Wisniewskj, W. Z. 1966, Comm. Lunar Planet. Lab., 4, 99

Kennicutt, R. C., Jr., et al. 2003, PASP, 115, 928

Kimeswenger, S. 2005, in High Resolution Infrared Spectroscopy in Astronomy, Proc. ESO Workshop, ed. H. U. Käufl, R. Siebenmorgen, & A. F. M. Moorwood (Berlin: Springer), 411

Klaas, U., et al. 2003, in The Calibration Legacy of the *ISO* Mission, ed. L. Metcalfe et al. (ESA SP-481; Noordwijk: ESA), 19

Koornneef, J. 1983, A&AS, 51, 489

Krist, J. 2002, Tiny Tim/*SIRTF* User's Guide (Pasadena: SSC)

Kurucz, R. L. 1993, Kurucz CD-ROM 13, ATLAS9 Stellar Atmosphere Programs and 2 km/s Grid (Cambridge: SAO)

Meixner, M., et al. 2006, AJ, 132, 2268

Price, S. D., Paxson, C., Engelke, C., & Murdock, T. L. 2004, AJ, 128, 889

Reach, W. T., et al. 2005, PASP, 117, 978

Rieke, G. H., et al. 2004, ApJS, 154, 25

———. 2005, ApJ, 620, 1010

Schulz, B., et al. 2002, A&A, 381, 1110

Skrutskie, M. F., et al. 2006, AJ, 131, 1163

Stansberry, J. A., et al. 2007, PASP, 119, 1038

Su, K. Y. L., et al. 2006, ApJ, 653, 675

Tokunaga, A. T. 2000, in Allen's Astrophysical Quantities, ed. A. N. Cox (4th ed.; New York: Springer), 143

Werner, M. W., et al. 2004, ApJS, 154, 1